Knowledge-Based Systems 328 (2025) 114166

Contents lists available at ScienceDirect

Knowledge-Based Systems

journal homepage: www.elsevier.com/locate/knosys

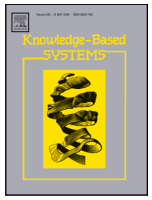

Deep learning event detector from long-term signal variation for seismic activity warning out of Schumann resonance

Carlos Cano-Domingo [a,b], Ruxandra Stoean [c,d,e,*], Manuel Soler-Ortiz [f], Nuria Novas [f], Manuel Fernández-Ros [f], Gonzalo Joya [g], Jose A. Gázquez Parra [f]

[a] Department of Computer Science, Universitat Politecnica de Catalunya, Carrer de Jordi Girona 31, Les Corts, Barcelona, 08034, Spain
[b] Barcelona Supercomputing Center (BSC-CNS), Plaça Eusebi Güell, 1-3, Barcelona, 08034, Spain
[c] Department of Computer Science, University of Craiova, A. I. Cuza 13, Craiova, 200585, Romania
[d] Artificial Intelligence and Machine Learning, Romanian Institute of Science and Technology, Saturn 24–26, Cluj-Napoca, 400504, Romania
[e] Department of Computer Science, West University of Timişoara, V. Pârvan 4, Timişoara, 300223, Romania
[f] Ceia3, Departamento de Ingenieria, Universidad de Almeria, Ctra. Sacramento s/n, Almeria, 04120, Spain
[g] Departamento Tecnologia Electronica, Universidad de Malaga, Campus de Teatinos, Malaga, 29071, Spain

ARTICLE INFO

Keywords:
Deep learning
Event detection
Warning system
Schumann resonance
Seismic activity

ABSTRACT

Deep Learning (DL) has shown capability in many areas of impact on everyday life. The paper proposes a DL architecture tailored for event detection from examining the time evolution of a signal. With temporal characteristics extracted by a *Convolutional Neural Network* (CNN) encoder and fed as input to a recurrent neural network, the model targets the detection of a possibly occurring investigated event in the given time interval. The utility of DL methodologies to solve physical problems is demonstrated for an application of the complex experimentally-studied existing interaction between *Schumann Resonance* (SR) and seismic activity. SR signals are electromagnetic waves propagating along the Earth-ionosphere cavity. Intense lightning activity is continuously present at the same locations around the world, being sensitive to physical perturbation. Seismic activity modifies this steady lightning pattern. The new DL model is applied to answer the research question of whether the variation of the SR signal is truly a verifiable forerunner of seismic activity. Several parameter configurations are explored, either model-related or linked to criteria for selecting seismic events. Results show preliminary evidence about the relation between distance-intensity space and SR perturbation, and provide valuable corroboration about the sensitivity of the sensor to a specific azimuth between the observatory and the *Earthquake* (EQ) epicenter, hence argumentatively supporting the SR temporal characteristics as an early seismic warning. This is the first generalization of seismic disturbance as a derivative of the SR, based only on its signal time series variation, as a hypothesized precursor of the EQ event.

1. Introduction

Deep Learning (DL) has become a permanent actor of real-world modeling, with a wide range of applications in various fields. Its strong capabilities also specifically target signal processing in domains such as medicine [1–4], physics [5,6] and energy systems [7–9]. These advances demonstrate the versatility and effectiveness of DL methods in extracting information from signal data.

In this article, we propose a DL methodology for yet another application toward signal processing. The research question we try to answer is whether seismic activity can be adequately detected from potential warning signals given by the temporal evolution of *Schumann Resonance* (SR) electromagnetic waves that circulate along the Earth-ionosphere cavity and if these can be discovered by DL.

The motivation for the current investigated hypothesis stems from the fact that the SR field has gained a huge interest driven mainly by two factors: i) the deployment of a large number of new *Extremely Low Frequency* (ELF) observatories (waves < 300 Hz) [10], and ii) the possibility to tackle the problem with more complex models i.e. by *Machine Learning* (ML) [11]. The current attention in the SR field is centered on two aspects: i) detection and study of the regular variation of each observatory, for example in Portishead (UK) [12], in the Artic and Antartic [13] or in Epirus (Greece) [14], and ii) linking the SR variations to other natural phenomena, such as geomagnetic storms [15], energetic

* Corresponding author.
E-mail address: ruxandra.stoean@inf.ucv.ro (R. Stoean).

https://doi.org/10.1016/j.knosys.2025.114166
Received 2 April 2025; Received in revised form 20 June 2025; Accepted 21 July 2025
Available online 29 July 2025

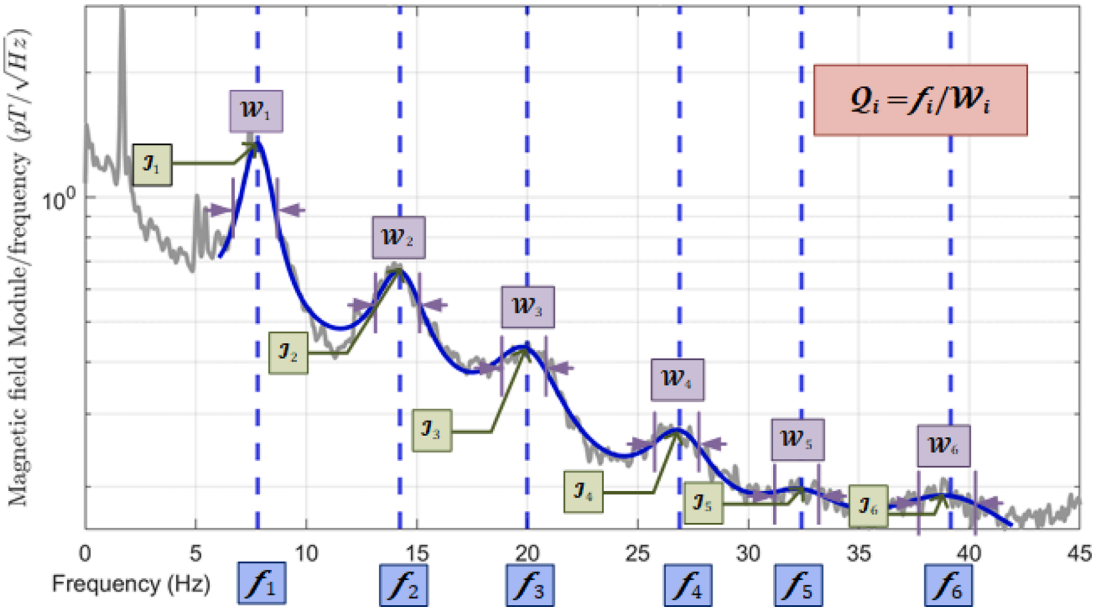

Fig. 1. Spectrum of SR signal with the most relevant parameters for each SR mode: f_i: peak frequency, W_i: Full width at half maximum, I_i: peak intensity, Q_i: Q-factor.

solar effect [16] or lightning activity [17], bearing human and economic impact [18–20].

Moreover, in this line, the relationship with *Earthquake* (EQ) events has attracted the attention of the scientific community. EQs are the releases of energy accumulated in the Earth crust, mainly due to friction between tectonic plates. This violent release creates seismic waves [21]. The intrinsic nature of the phenomenon that provokes the sudden liberation of energy in an EQ is a challenging field to understand, mainly due to irregular forces at an unpredictable time. For this reason, it is possible to consider that every EQ can be seen as an unrepeatable event resulting from the distinct interaction of many factors, since each EQ is a unique event, although the results of EQs as ground motions tend to be similar. Specifically concerning the SR-EQ connection, there is evidence of some detectable perturbations in the Earth-ionosphere electromagnetic cavity before and after the release of an EQ. Studies across multiple regions and different stations (Middle America, Europe, Asia) have noted this relationship looking at EQs taking place 10 years apart [22,23].

The energy of the system is mainly produced by continuous discharges of lightning across the Earth [24]. Due to the impulse response of the Earth-ionosphere cavity, the waves that correspond to its resonance frequencies persist. The fundamental frequency and its five lower modes are around 7.8 Hz, 14 Hz, 20 Hz, 26 Hz, 33 Hz and 39 Hz [12]. As can be seen in Fig. 1, SR can be characterized by the parameters of each mode, which can be summarized in three: I_i) Intensity value, f_i) Frequency value, and Q_i) Q-factor. The intensity value is strongly correlated with the intensity of the lightning activity. The frequency of each mode depends on the location of the lightning activity relative to the observatory and the conditions of the electromagnetic cavity. Asymmetries play an important role in this aspect; the Q-factor is the relationship between the energy accumulated in the cavity and the energy dissipated in each cycle. This factor is highly dependent on the height of the ionosphere and its composition [25,26]. Ogawa proposed a simplified analytical solution for the Q-factor in 1970 [27] (Eq. (1)), where Q is the Q-factor of the SR, ω_o the SR angular frequency, μ the permeability cavity, σ the conductivity of the ionosphere and h the height of the ionosphere. It can be observed that there is a strong dependency between the Q-factor and the ionosphere conductivity, which corresponds to the virtual height of the ionosphere.

$$Q = h \cdot \sqrt{2 \cdot \omega_o \cdot \mu \cdot \sigma} \tag{1}$$

In light of all of the above, the contribution of the proposed methodology is a new DL architecture that explores SR parameters for a warning EQ system using a long-term period (5 years). The available data allowed us to work on this larger temporal frame, and thus objectively validate the behavior of the model over time. The proposed approach focuses on recognizing the time variation of SR characteristics and has been studied for sensitivity under different EQ conditions, for its potential towards early recognition. The approach proves the advantages of reducing the dimensionality of the signal spectrum and examines different DL architectures for SR variation analysis. These findings pave the way for further research in the field of EQ detection based on SR parameter precursors.

The leading theory in this respect is that the Mesoscale convective systems continuously produce high-intensity lightning discharges around a relative fixed location. A large EQ may change the electromagnetic state of the ionosphere, causing the SR signal to suffer progressive variations in the parameters - frequency and, consequently, Q-factor. Our hypothesis is that a DL model can learn the seismic pattern variation in the SR parameters when trained with long time series, assuming the appropriate approach is chosen and physical-based EQ criteria are followed.

The architecture introduced in this paper uses the outcome of a CNN encoder introduced in earlier research [28] that extracts the non-permanent characteristics from the SR signal. This resulting sequence of consecutive SR codes thus becomes the input of the proposed recurrent DL network - namely, a *Gated Recurrent Unit* (GRU) - while the EQ events are presented as the output. Through the multimodal data coupling between SR signals with known EQ events and their DL modeling through the novel approach, we thus show a new possibility of analysis of this valuable interrelation that could act as an early warning system.

The paper is structured as follows. Section 2 contextualizes the connection between EQs and their probable herald in the Earth spheres, as well as the DL entries in the field. Data collection and pre-processing are given in Section 3. The proposed method, in terms of mechanisms and considered problem characteristics, is described in Section 4. Section 5 presents the results obtained, along with the experimental setup. The findings are discussed in Section 6 and the final conclusions are reached in Section 7.

2. Literature review

Early warning strategies based on the ground signal produced by the energy release allow to minimize the consequences of an imminent EQ, by giving people the chance to reach a safe spot [29]. However, these systems only predict the impact of an EQ, but not their occurrence. Another approach is to analyze time series statistically or with ML techniques [30,31]. Although these techniques obtained encouraging results, the intricate nature of the EQ source makes the estimation based on historical data very unreliable.

Several efforts have been made to understand the mechanisms of coupling parameters among lithosphere, atmosphere, and ionosphere with EQ events. In [32], the authors analyzed the variation of six parameters related to the stated layers, from the subsurface to the lower atmosphere with respect to two strong EQs. The results demonstrate the quasi-synchronous coupling between these parameters prior to EQ events in Nepal. As an interesting result, it is possible to see the abrupt drop in surface air temperature immediately before the EQ event. Furthermore, in [33], the authors provide valuable evidence of the relationship between EQ events and the variation of the spatial distribution of surface and atmospheric parameters. They exposed the synchronous changes in the surface-atmosphere conditions in the stage of an EQ preparation and after.

Various works focus on studying the ionospheric precursors for monitoring the EQ activity [34]. A systematic review about the effect of EQ in the ELF band can be found in [35]. The aim is based on some compelling ideas such as i) ground and underground *Electro-Magnetism* (EM) waves can penetrate, propagate and reach the ionosphere, leading to a modification of their characteristics, ii) ionospheric disturbance may change up to 5 days before the EQ event or iii) the extension can occupy about 5°. Furthermore, post EQ anomalies in the ionosphere after EQ have been satisfactorily detected using *Global Navigation Satellite Systems* (GNSS) [36]. The Lincoln laboratory at MIT is currently developing a ML-based project, trained on ionospheric activity preceding an EQ [37]. Ionospheric perturbations were detected roughly 10 days before four EQs in a Chinese province [38]. In [39], ionospheric electron density was also observed 40 days before and 1–5 days after EQ in China, with electromagnetic signals detected seconds before the event. Two geomagnetic anomalies recorded from stations within an epicentral distance of 191km preceded by 7 months a large EQ in western China [40]. Ionospheric precursors of another EQ in China were also analysed in [41] to detect seismic anomalies.

The application of DL in the EQ field has been demonstrated to be an auspicious tool. The usage of an *AutoEncoder* (AE) based on an *Long Short-Term Memory* (LSTM) DL network is able to suspect the occurrence of an EQ based on the ionosphere data [42]. Furthermore, recent research has proposed a framework to estimate the EQ magnitude based on the LSTM architecture [43]. A monitoring system for early warning based on DL with an IoT network is shown in [44]. The system is able to detect the magnitude and the location of an EQ only 3 s after the events using an AE with a CNN architecture. Another example can be found in [45], where the authors proposed a novel methodology for parameter classification in an early warning strategy. A recent article also explores a complex DL architecture based on a compact convolutional transformer to predict the arrival of the P-waves and S-waves of an EQ [46]. Additionally, the work of [47] employs a CNN in an EQ prompt warning system, based on speed-of-light prompt elastogravity signals from Japan. As also demonstrated in many other practical domains of application dealing with signals and their temporal analysis, the current supremacy of DL as opposed to the classical time series approach stems from its simulation of the neural system and the capabilities of the current hardware to process numerous layers fed with a large amount of data. Moreover, its additional architectures for signal dimensionality reduction support its successful utilization in real-world applications, where noise and complexity are present.

Last but not least, several authors have tried characterizing the relationship between EQ events and the wave generated in the cavity, the SR. The detection of SR anomalies related to an EQ have been satisfactorily discovered in different locations around the globe in recent years: Japan [48], Mexico [49], and Greece [50]. In [26], the authors indicated its relationship with EQ of magnitude more than 7 and *Source-Observer Distance* (SOD) up to 3000 km. In addition, the effectiveness of SR records to be used as seismic precursors was studied in [51].

For a more visible positioning of the current research, the research matrix in Table 1 summarizes the main directions of the state of the art, from EQ detection to connection with geosphere changes (including SR), and from traditional approaches to ML and DL.

Within this conceptual context, the research gap in hypothesis and method filled by the present work is given by CNN encoded transient characteristics of the SR modeled by a *Recurrent Neural Network* (RNN), as a precursor of EQ events.

3. Data

The modality for data collection and processing is described in the following.

3.1. SR measurements

The SR signal was obtained through the observatory “Sierra de los Filabres”. It was developed by the research group TIC-019 University of Almeria. The system comprises two high-sensitivity orthogonal ELF sensors followed by a high-resolution acquisition stage. The observatory is entirely isolated from any human interference and has been continuously measuring since 2015. The SR data used for this investigation range from January 2016 to December 2020; a detailed explanation of the observatory is given in [10]. Data are collected in a 30-minute register, and a Lorentzian fit algorithm is applied to each segment to extract the most useful information. Information about the processing algorithm can be found in [52].

3.2. SR encoding

The SR signal presents a recurrent shape that is more or less identical for each register. On top of that, some changes related to the parameters take place because of different conditions. To focus on the time variability of the SR signal, it is essential to remove the part of the signal that is very common between sequential days. In previous research [53], we developed a DL encoding that reduces the SR spectrum to only ten values per register. These ten values represent the SR signal variation, but not the standard shape. From this encoding, the DL architecture can decode the signal with minimal loss. Reducing the number of variables is an important aspect to allow the DL time series detector to focus on the time evolution of the signal. The results showed a solid improvement over the raw SR spectrum [28]. A general view of the encoder can be seen in Fig. 2. The encoder reduces the input from 256 components, corresponding to the SR spectrum, to 10 codes. A randomization layer is added to allow generalization [54]. The three convolutional layers use a kernel size of 3 and stride 1 so that each filter spans roughly one quarter of the fundamental SR mode (~8 Hz), capturing local spectral variations without losing frequency resolution. To improve the performance of the DL EQ detector, a standardization process is needed. The mean value of the SR mean code is set to 0, and the standard deviation of the SR standard deviation codes is set to 1.

3.3. Seasonality normalization

Although the canonical SR spectrum is remarkably stable, its amplitude slowly drifts with the solar-controlled ionospheric conductivity, leading to pronounced diurnal and seasonal envelopes. The variational AE itself acts as a data-driven high-pass filter: because its decoder

Table 1
Research matrix of condensed related literature context.

Entry	*Concept*	*Hypothesis*	*Method*	*Findings*
[31]	Hazard analysis, damage detection	ML approach	Survey of models	ML potential for EQ analysis and management
[30]	Nowcasting EQ	EQ cycle analysis	ML: Clustering, EMA, PCA, *Random Forest* (RF)	Signals detected in a correlation time series corresponding to EQ
[33]	Surface / atmosphere linked parameters	Correlation of satellite observation data with EQs	Anomalous background variation	Atmospheric changes before EQs
[39]	Lithosphere, atmosphere, ionosphere changes	Modifications in the geospheres before EQs	Mean and standard deviation, Anomaly detection	Geolayers interaction before EQs
[41]	Atmospheric-ionospheric precursors	Variations before EQs	Anomaly detection, wavelet transformation	Irregularities in the seismic preparatory phase
[43]	EQ magnitude prediction	Seismic station providing information	DL: LSTM	Competitive estimation, even with remote station
[46]	EQ waves phase-picking	Seismogram analysis	DL: CNN Transformer	Production-ready accuracy
[48]	SR- EQ link	SR anomaly prior and after EQ	Riccati and 2D telegraph equations	Intensity of all SR modes
[49]	SR- EQ connection	SR anomaly around the seismic event	Anomaly detection	Frequency and amplitude anomalies

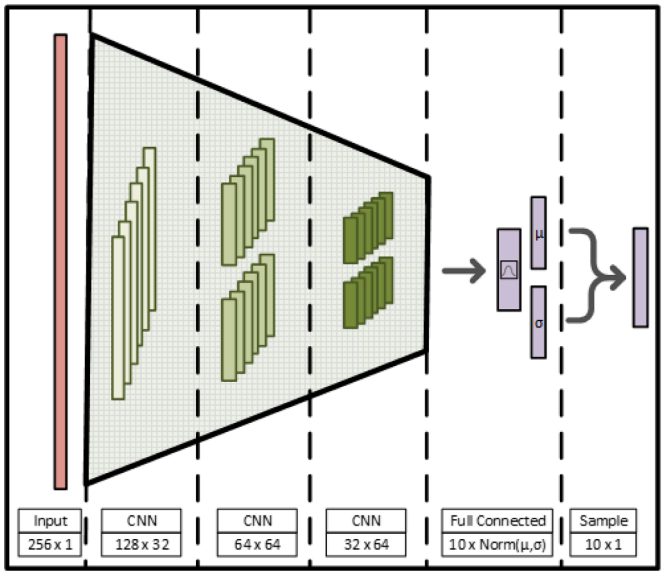

Fig. 2. DL encoder architecture. It is composed of three convolutional layers, followed by a fully connected layer with 20 outputs, 10 outputs for the mean and another 10 outputs for the standard deviation of each code.

learns the recurrent SR template, the 10 latent codes are forced to represent *only* cycle-to-cycle deviations for the complete training protocol [55,56]. This normalization ensures that the daily and seasonal periodicity does not leak into the time series detector.

3.4. SR latent embedding pre-processing summary

Each 30-min ELF spectrum is first decomposed by a 6-mode Lorentzian fit that isolates the normal cavity modes. The resulting envelope is then compressed by a denoising AE that maps the 256-bin spectrum to a 10-value latent code. Training on spectra intentionally corrupted with low-level Gaussian noise yields a representation robust to common environmental and instrumental disturbances. Previous validation shows a reconstruction error below 2 % for clean data and below 4 % for noisy segments, sufficient for the present work, which relies only on the temporal differences $\Delta \mathbf{z}_t$ between successive codes. A further *Kolmogorov-Smirnov* (KS) test confirms that the latent-code distributions of clean and noisy registers are statistically similar; therefore, retaining the estimated codes, even when noise is present, is preferable to discarding the affected segments, as it preserves the continuity required by the downstream time-series detector.

3.5. EQ data

The EQ database was obtained using data from the United States Geological Survey. This US Agency gathers information about all EQs with a magnitude greater than 4.5. We have collected information on every EQ that occurred between the start of 2016 and the end of 2020. The EQ data have been acquired through a public EQ Repository [57]. For each EQ, we have obtained the exact location, the origin intensity (measured on the Richter magnitude scale) and the depth. The location has been used to compute the SOD and the azimuth. EQs can be produced on the surface of the crust and deep below the crust.

The complete USGS catalogue for the study period (2016–2020) lists 35 023 EQs with magnitude $M \geq 3.0$. Because not every event is expected to produce a detectable SR perturbation at the Sierra de los Filabres observatory, we applied a pragmatic distance-magnitude filter: only events whose epicentral distance is small enough–relative to their magnitude–to exceed a fixed *magnitude-distance score* were retained. This criterion reduces the working set, providing a better-balanced dataset while preserving the events most likely to leave an ELF footprint in the observatory records. Investigating whether the proposed system can learn to focus on an even more informative subset is left to later sections of the manuscript. From the events detected, we retained three for validation. To ensure sufficient training data, we excluded the first three years of recordings from candidate selection. We then ranked the top 20 earthquakes based on a relevance score combining moment magnitude and epicentral distance. To avoid outliers, the three highest-scoring events were discarded, and three events were randomly selected from the remaining 17. These selected earthquakes were excluded from every training fold and used exclusively for validation.

4. Methodology

The general idea is to recognize the time during SR evolution to detect possible ELF perturbations produced by EQ events. Due to the inherent difficulty of characterizing the impact of an EQ in the ELF band, the proposed architecture contains a high degree of flexibility. One of the expected impacts of this methodology is the provision of different models of EQ predictors using the explored parameter characterization for future research developments in this area.

4.1. General architecture

The time slot considered in this investigation is the 30-min segment of each SR distribution code, so the EQ database has to be adjusted to that of our observatory. Each EQ is suited in one SR time slot. However, it is not possible to know the duration of the EQ perturbation, so each

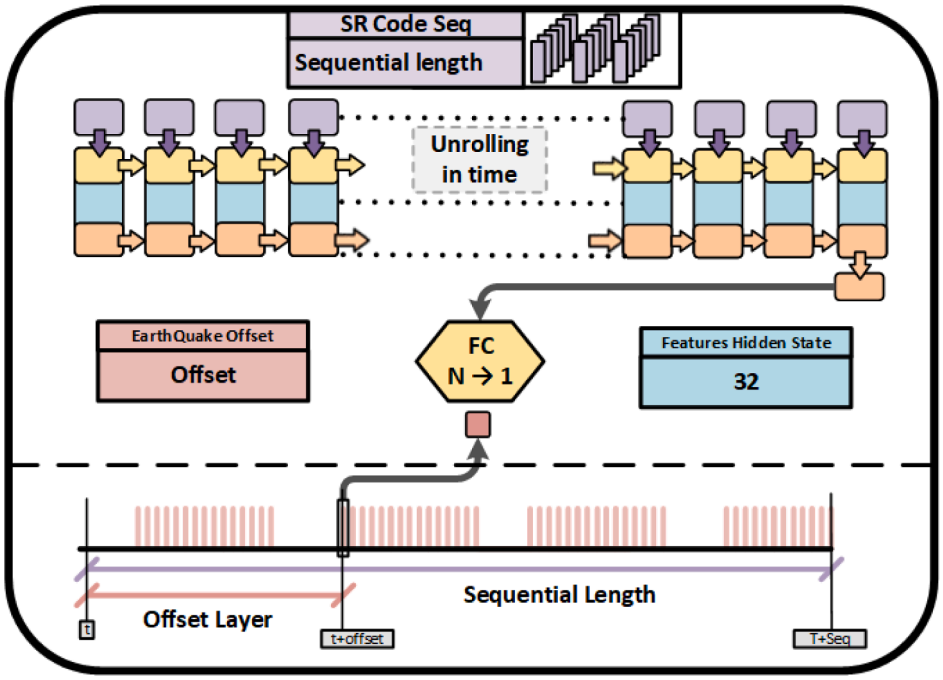

Fig. 3. General scheme of the proposed DL architecture.

one of the EQ responses has been increased from a one-time slot (30 min) to more, depending on the values (6 – 24 h).

The input of the system consists of the SR distribution codes resulting from the CNN encoder [28]. Each code is composed of mean and standard deviation values corresponding to a Gaussian probability distribution. The input consists of a sequence of SR codes. The number of SR codes that make up a sequence is a parameter of the methodology. The entire data sequence is fed to a RNN network. The network's first step is to sample one SR code for each SR distribution code. This is done following Eq. (2), where n is each input of the batch, μ_n and σ_n are the values associated to one SR distribution code and x_n the input of the RNN cell.

$$x_n = Norm(\mu_n, \sigma_n) \tag{2}$$

The central RNN cell is a bi-directional GRU network composed of three layers, with a dropout of 0.5 between them. This cell will be explained in Section 4.3. The state of the final layer of the Bi-directional GRU cell is connected to two fully connected layers with a dropout of 0.5. The first fully connected layer takes the output state, performs a dropout, and connects to 128 values as its output. The next layer takes the 128 values and outputs a single value. After the completed input sequence is fed to the network, the system calculates the expected output, which is a single value related to the occurrence of the EQ in the time interval corresponding to the middle of the SR sequence. For example, if the sequence length is 1440, the expected output corresponds to the SR EQ influence at the time slot 720. Even when the EQ perturbation is widened, the number of ones in the output (EQ perturbation) is much lower than that of the zeros (non-EQ perturbation), so the algorithm would learn to reduce the error by always predicting a zero. To avoid this problem, the inputs of the training step are chosen randomly with the same probability of taking one sequence as a zero-sequence. An image of the general architecture can be seen in Fig. 3.

The loss function used in this methodology can be seen in Eq. (3), where n is each input of the batch, l_n the calculated loss, y_n is the ground-truth output, S is the sigmoid function, and x_n is the sampled version of the input. The Sigmoid function obtains a value of 0 or 1 from a continuous output.

$$l_n = \left[y_n \cdot \log(S(x_n)) + (1 - y_n) \cdot \log(1 - S(x_n))\right] \tag{3}$$

4.2. EQ parameters

As commented above, the absence of a clear definition on the relationship between EQ and SR makes this research complex. There are several possibilities to model this influence, and the system can explore which combination fits better for predicting the EQ event in the SR signal.

4.2.1. EQ selection

One aspect is to select criteria from the EQ characteristics. The system may only be able to detect the closest ones, the most intense ones, or within a specific arc. Three parameters will be compared: magnitude, distance between the observer and the EQ event and angle between the observatory and the EQ event. Magnitude and SOD are correlated parameters. The more intense an EQ is, the further a seismograph detects the seismic event. We hypothesized the same idea for the ELF data and explored the perceptibility radius [58]. Its general formula can be found in the literature Eq. (4).

$$D = 10^{A \cdot M + B} \tag{4}$$

M stands for the magnitude, D for distance. However, the values of A and B are broadly different from those of the seismic sensor, because the propagation constant of the ELF band is entirely lower than the mechanic one in the seismic field.

The *perceptibility curve* defines whether an earthquake of a given magnitude could realistically be detected at a given distance. This curve is defined in log-log space as $\log_{10}(D) = A \cdot M + B$, where the coefficients A and B are computed dynamically, using two reference points in the magnitude-distance plane. The first reference magnitude M_{start} corresponds to a distance $dist_{start}$, and the second magnitude is defined by adding M_Δ to the first, with its corresponding distance being $dist_{start} + dist_{delta}$. These two points define a straight line in log space that is used to compute whether an earthquake falls within the detectable region: specifically, whether its actual distance is less than

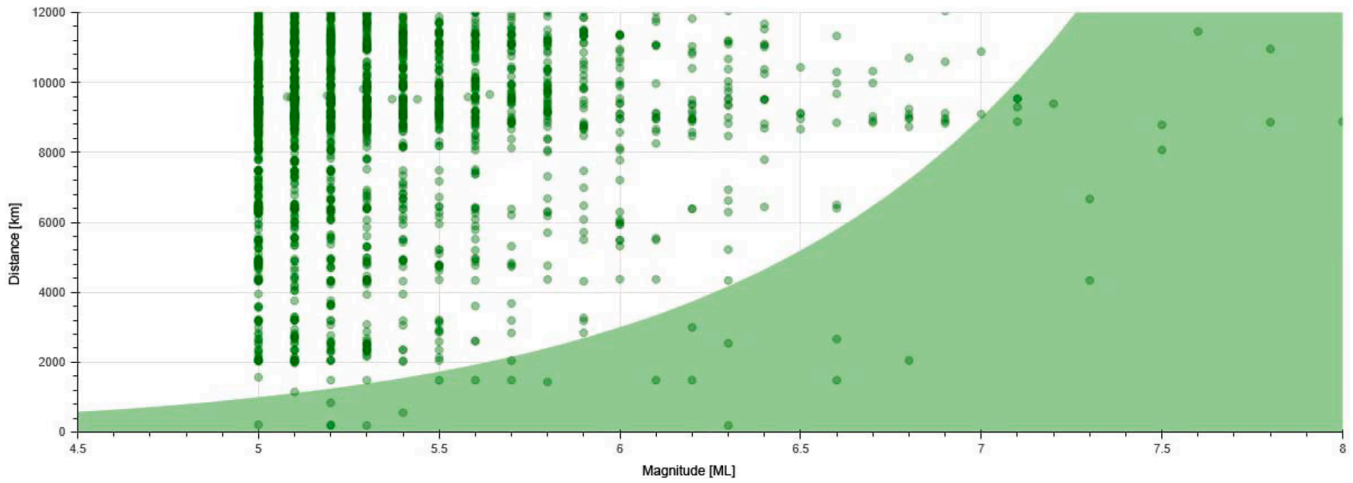

Fig. 4. Perceptibility radius with A = 0.47 & B = 2.38.

or equal to $10^{A \cdot M + B}$. If the condition is satisfied, then the event is considered.

An example can be seen in Fig. 4.

4.2.2. EQ perturbation in ELF records

Another aspect is the time interval around an EQ in which a perturbation can be detected using SR data; the time evolution of the SR signal has to be monitored to detect the variations associated with the event. According to the literature, perturbations have been identified more than ten days before and five days after the event. We select multiple values in 2.5 day steps before and after the EQ. We have called it *Sequence length*.

In the seismic field, the duration of the EQ is usually less than 1 min. Although the effect in the ELF spectrum is not determined, a more extensive repercussion in the ELF field can be expected. We have set this variable *EQ windows* as a parameter and test the values between 6 h and 24 h.

4.3. DL cells

The central DL cell used in this research is the bidirectional GRU. A GRU cell presents the advantage of having the memory unit combined along with the network and fewer gates, so the number of parameters can be decreased without substantially reducing performance. Furthermore, the bidirectional architecture can be used when the system allows an offline mode, which is when the complete sequence is known before the start, as in this case. To compare with other cells, different architectures have been chosen: CNN with 1 dimension and ten channels, CNN with two dimensions $10 \cdot sequence\_length$, LSTM and unidirectional GRU.

4.4. Detection performance

The aim is to measure the detection (or recognition) success ratio of the EQs. But, as it was exposed in the introduction, the detection of EQ using the SR signal is not an easy task; the impact of an EQ in the ELF band is not formally characterized in the literature. Therefore, the classification of EQ in their relation with the SR signal has not been sufficiently modeled. Also, it is challenging to know which ones can be perceived. It is also important to remember the unbalanced expected result, with much more predicted values of 1 than for 0, so the system has to learn the same pattern when the number of EQs is small. The proposed architecture has been trained and validated under several configurations with different sets of parameters. Every time the configuration parameter values are restarted and a new training process begins is called a realization.

To select the validation data set from all the SR codes sequences, three EQs have been randomly chosen in each setup, as detailed under subsection 3.5. Therefore, each realization has its EQ selection. All sequences that have at least one value of this EQ have been removed from the training data set. To extract the metrics, the SR code sequence of these EQ has been chosen along with several sequences surrounding the EQ, most of them zeros. These SR sequence codes are gathered and compose the validation data set.

To solve this problem, three primary approaches have been used: i) to discard all the iterations when the training loss or the validation loss is lower than the stopping threshold; ii) to discard all the realizations which have more ones than zeros in the validation data set; and iii) to detect when the model has predicted the EQ with at least 1 value.

An example of a validation data set with two predictions can be seen in Fig. 5. The number of EQs is set to 3, but there are a few values at the end of the validation data set. This effect is caused by randomly choosing three EQ and the points surrounding them. Sometimes, there is an EQ very close to another.

Due to the random choice of three EQ, some realizations could have a higher probability of correctly predicting the output than others. The chances of detecting EQs are not established, but it can be guessed that not all EQ have the same impact on the ELF band. Hence, several realizations with the same configuration have been performed to extract experimental evidence with statistical support.

Recognition ratio. For every realization, we keep three unseen earthquake (EQ) events as validation targets. An event is considered a candidate EQ when the reference mask remains positive for a sufficient number of samples (at least half the expected window length, $L_w/2$). The recognition ratio (RR) is then defined as

$$\mathrm{RR} = \frac{N_{\mathrm{detected}}}{N_{\mathrm{EQ}}} \tag{5}$$

where N_{EQ} is the number of candidate earthquakes (three in our setup) and N_{detected} is the subset for which the model produced a positive response in the corresponding interval. This metric is computed independently for each realization and then aggregated over multiple runs with the same configuration to assess performance stability.

To quantitatively assess the similarity between the values of the different parameters, we used the KS test [59], where the lower values represent a more likely common origin. This test measures whether two samples could have been obtained from the same distribution with the

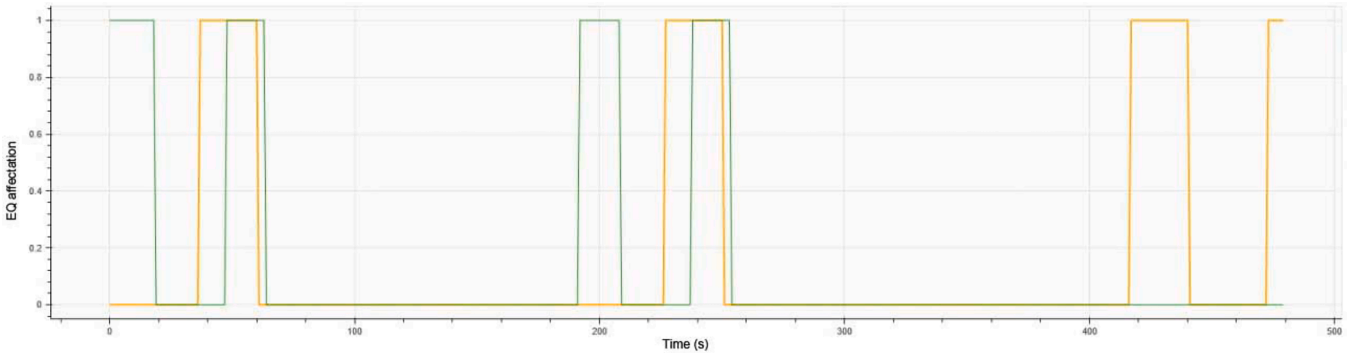

Fig. 5. Example of a validation data set with 3 real EQs (in orange) and two detected (in green). X-axis represents the time in steps of 30min and y-axis EQ presence. Three validation sets are represented together.

Table 2
Initial sweep parameter configuration values.

Variable	Values range	Step
Sequential Length	[240 – 1920]	240
EQ Window	[12 – 48]	12
Azimuth	[15° – 90°]	15°
Distance Start	[1000 km – 4000 km]	1000 km
Distance Delta	[1000 km – 4000 km]	1000 km
Distance Max	[4000 km – 16000 km]	2000 km

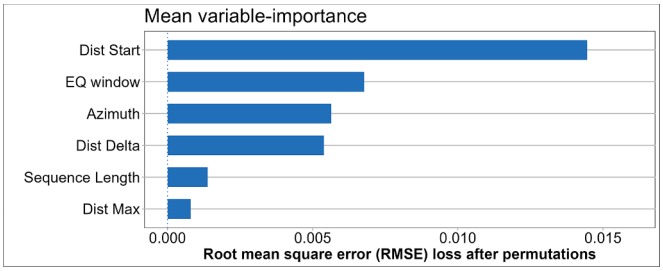

Fig. 6. Variable significance for the initial configuration sweep.

null hypothesis. In the figures on the experimental results in Section 5, we have included the KS value, which corresponds to the p-value of the null hypothesis. A KS value of 0.049 shows enough evidence to consider that the two configurations represent different models with 95 % confidence.

5. Results

The focus of this research is to explore the feasibility of detecting EQs in the SR signal using DL, along with establishing a set of parameters that can be used in future scientific works for different architectures. As mentioned in the previous section, the approach used was to randomize the EQs to be predicted, and average the realization to find the best parameters for the model. A sequential path has been followed, starting with the stages used in previous research [28]:

1. Selection of the problem-related parameters of the approach: sequential length, EQ window and the position in the sequence length to detect the EQ.
2. Relation between SOD and Magnitude in EQ detection using SR.
3. Importance of the azimuth between the EQ epicenter and the observatory.
4. Comparison with other DL architectures.

5.1. EQ parameters

As a first attempt to find the best configuration of the EQ-related variables, a combination of 6 parameters has been used. This first subsection investigates their influence. The parameters can be seen in Table 2.

The first column indicates the parameter name, the second column the limits of its value, and the last column the interval between consecutive values. As an example, the *EQ window* possible values are: 12, 24, 36 or 48.

The total number of models trained is 872, including those without convergence. It is possible to know the relative importance of each parameter in relation to the success ratio obtained (percentage of EQ detected on total EQ in the validation data set) using an explanatory model over a regression. A *Gradient Boosting Machines* (GBM) ML model [60] has been used in conjunction with DALEX [61] to understand the results. In Fig. 6, the variable importance of each parameter in the initial configuration is shown. It can be seen that the minimum SOD value is followed by the EQ window. The sequence length is less relevant than expected.

To remove the variance introduced by parameter permutation, some parameter values were fixed while studying their individual impact. Sequence length is the first to be fixed. The ratio obtained in each realization with the same sequence length was averaged, and the results can be seen in Fig. 7(a). Due to the high number of different combinations included in each group of realizations, the success ratio is relatively low and there is no substantial difference between the groups. However, the best values are obtained using the value of 1200. In order to discuss the EQ window, only realizations with a sequence length of 1200 will be used; the number of realizations that fulfill this criterion are 89. The results are not conclusive enough to ensure statistical difference between groups, except for the 12 EQ window value, based on the KS test over the 24 EQ value, as it can be seen in Fig. 7(b).

The offset for EQ detection is the position in the sequence in which the system predicts the EQ. To compare the possibilities for the model, the first configuration of EQ parameters will be used; more than 5 of magnitude and distance less than 3000 km. The result can be observed in Fig. 8. The symmetric pattern around the 0.5 value is clear, which is consistent with the bidirectional system used in this research. In the following, an offset label of 0.05 will be used, that is, at the beginning of the SR sequence.

5.2. Relation between SOD and magnitude in the detection

Based on the results obtained in the prior subsection, in this part the criteria used for selecting EQs will be explored. The previous results set the following configuration: i) sequence length 1200; ii) EQ window 24 and iii) offset ratio 0.05 %. In this analysis, a maximum azimuth of 45° was chosen. As mentioned, the most important parameter seems to be the start distance related to the selection of EQ. A sweep configuration for this parameter can be seen in Fig. 9(a). The results show no clear differences between 3500 km and 4000 km. However, significant differ-

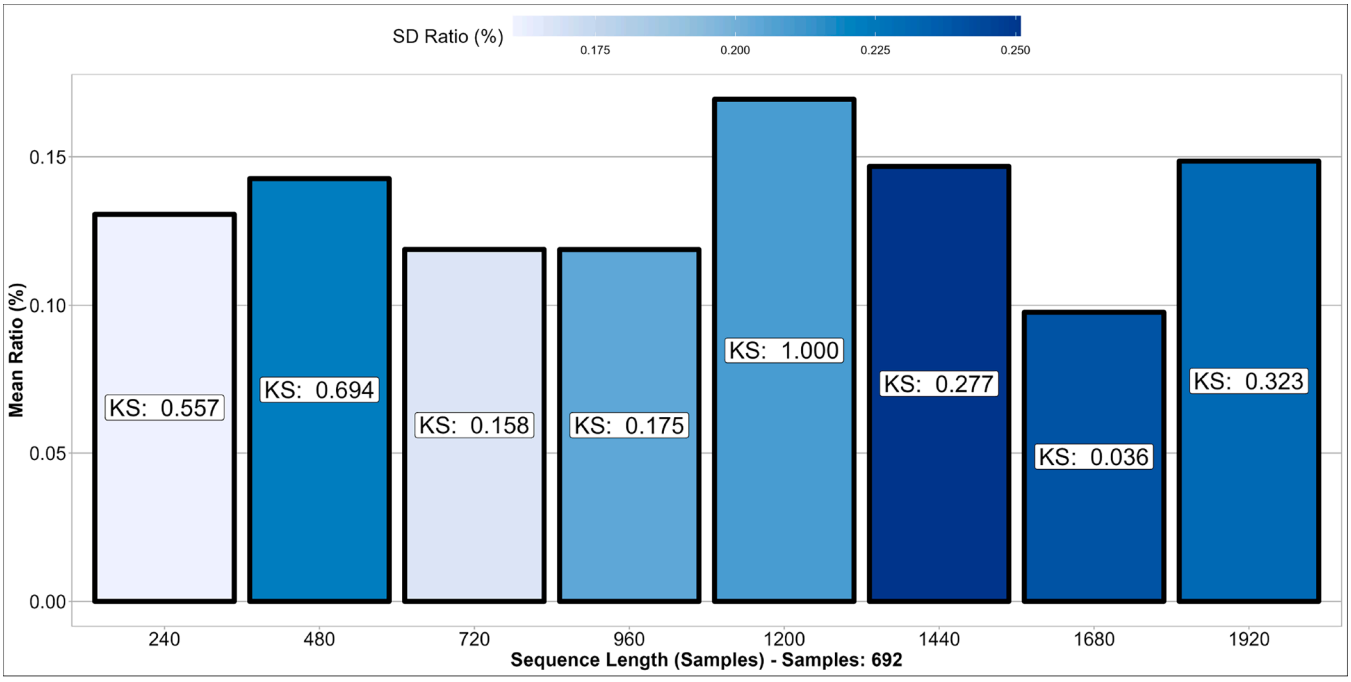

(a)

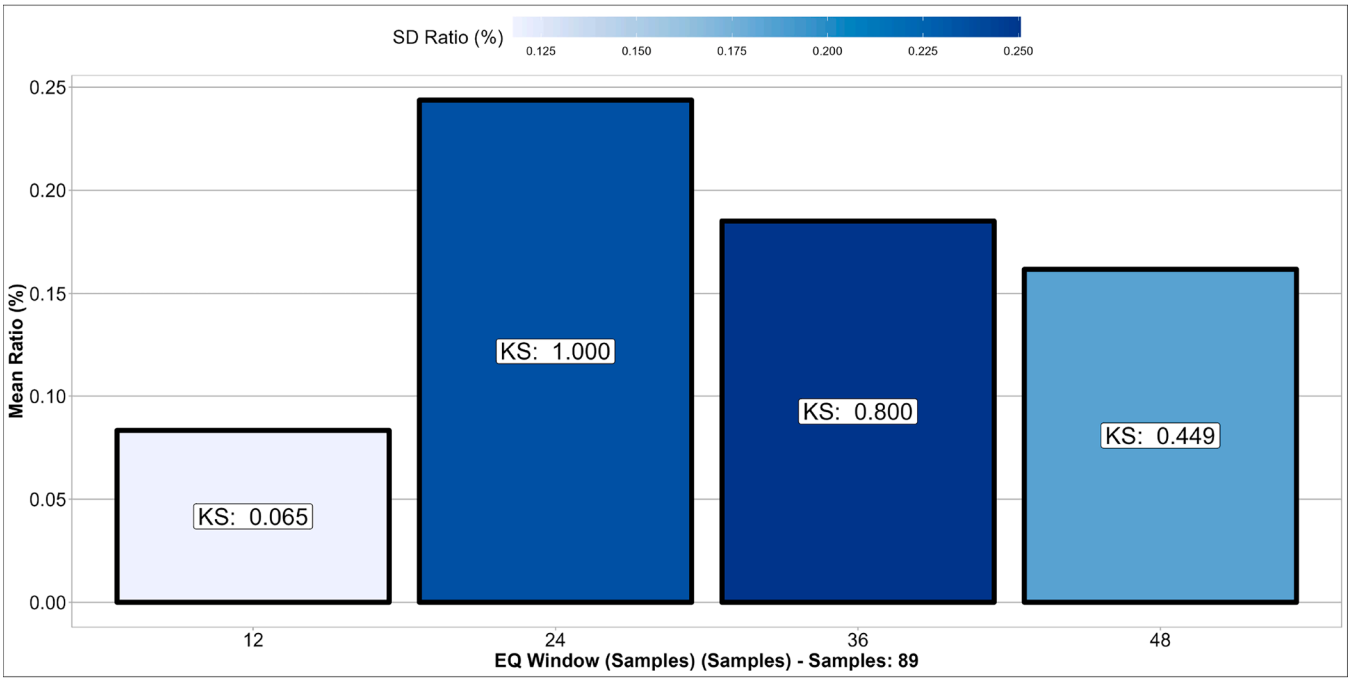

(b)

Fig. 7. Mean ratio obtained for each group. KS is the p-value of the KS test between the selected group and the others. The color intensity represents the SD ratio. (a): Group based: Sequence Length, reference KS: sequence length = 1200. Realizations: 692. (b): Group based: EQ windows, reference KS: 24, filter to sequence length = 1200. Realizations: 89.

ences can be seen for the rest of the groups. It can be determined that 1000 km, 2000 km and 3000 km are not the same model as the reference (4000 km) with 95 % confidence. It is also important to note that 2500 km presents a mean ratio similar to the reference, but SD is substantially higher, around the double of the reference. In light of these results, the next step is to determine the best value for SOD at the second point, using a value of 4000 km in the first.

Due to the high variability of the system, there is no clear pattern. Just as well, the results of the KS test are not solid enough to reject the hypothesis that all groups are taken from the same model, as can be seen in Fig. 9(b). However, considerable differences can be extracted, such as the worst result for the 3000 km group. The best result has been obtained with a distance delta of 4000 km. The last part for selecting EQ based on SOD and magnitude is decided if a limit in the maximum SOD

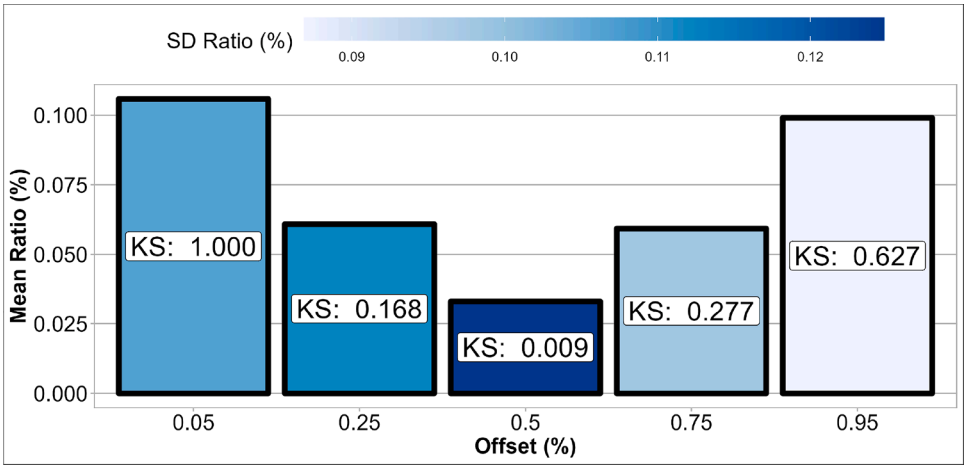

Fig. 8. Mean ratio obtained for each offset value from 0.05 to 0.95. KS is the p-value of the KS test between the offset equal to 0.05 and the others. Color intensity represents the SD ratio.

is needed. This could happen because the formula associated with the perceptibility radius increases exponentially on the second coordinate. In Fig. 9(c), it is possible to notice a symmetrical pattern in which the best results are related to the extreme values, 6000 km and 14000 km. The KS is not conclusive since the p-value is higher than the minimum needed to discard the null hypothesis, but it is very likely that the extreme values are not related to the middle one, 10000 km. The SD ratio is also interesting because the first category does present a similar mean value to the last, but SD value is doubled, so the best result can be seen when the maximum allowed SOD is 14000 km. The best selection for the coordinate space can be seen in Fig. 10.

5.3. Importance of the azimuth between the EQ epicenter and the observatory

The criteria for selecting EQs is based on the assumption that the best result can be achieved when the azimuth between the ELF observatory and the EQ is less than 45° [62]. However, a robust analysis is needed to explore the best options to detect EQ occurrence. In this analysis, a wide range of maximum azimuth values for the *North-South* (NS) sensor is examined. The minimum azimuth is 15° and the maximum is 90°, which corresponds to all values. Since the sensor under study is the NS, the azimuth is in correspondence over the parallel. The results can be observed in Fig. 11, showing that the maximum value is found with a maximum azimuth of 60°. These results have to be carefully inspected because the maximum azimuth limits the number of EQs that the system has to learn. Therefore, an optimal number of values can be obtained when the maximum azimuth is 60. To support the validity of this approach, two different orientation of the EQ selection have been selected. It is expected that the NS sensor is more sensitive to the EQ produced in the coordinates where the sensor has the highest value of its radiation diagram, perpendicular to the coil axis. These two orientations can be seen in Fig. 12. In Fig. 12(a), the criteria used for selecting EQ correspond with the maximum radiation reception obtained by the NS sensor: in red the maximum azimuth allowed of 60° over the parallel, and in blue with 30°. In Fig. 12(b) the sensor is orthogonal to the EQ detected. The main aim of this approach is to compare whether there is a particular sensitivity for EQs in orientation. The results can be seen in Fig. 13. Fig. 13(a) corresponds to a maximum azimuth allowed between the observatory and the EQ of 30°, and Fig. 13(b) corresponds to the maximum azimuth of 60°. It is possible to see that the NS sensor obtained considerably better results when the EQs to detect are aligned with the maximum sensor sensitivity for both cases, 30° and 60°. As exposed previously, performance improves when the maximum azimuth allowed is 60° compared with a maximum azimuth value of 30°. This is again validated when the orthogonal orientation for selecting EQs is used. The results are also supported by the KS values; there is enough evidence to confirm that the system is sensitive to EQs with more than 99 % confidence.

5.4. Comparison with other DL architectures

To provide a comparison between different DL architectures for the current task, five DL models have been selected:

- GRU: RNN that uses gating mechanisms to regulate the flow of information and persistence of memory in the network.
- BI-GRU: Bidirectional version of GRU that processes sequential data from past to future and future to past, resulting in better performance on tasks with bidirectional dependencies.
- LSTM: RNN that uses an internal memory cell and gates to handle long-term dependencies while retaining information from the near past.
- CNN-1D: is a 1D CNN designed for processing 1-dimensional data such as sequences of text or audio signals. It has difficulty in capturing long-range dependencies.
- CNN-2D: is a 2D CNN designed for processing 2-dimensional data such as images. Now, this network is used as a spectrogram detector using the codified version of the SR spectrum. The main disadvantage is the difficulty to detect long-term dependencies.

5.4.1. EQpred common backbone

All variants start from the same two-stage design. The network receives a multivariate sequence $\mathbf{X} \in \mathbb{R}^{T\times 10}$, where the 10 channels correspond to the synchronized seismic sensors and T is the window length (2 000 samples, 20 s in our experiments). First, a *feature extractor*–chosen among a family of recurrent or convolutional networks–maps the input to a fixed-length vector $\mathbf{h} \in \mathbb{R}^{d_{\text{feat}}}$. Second, a lightweight regression head produces the final scalar output (EQ probability to the next event). For uni-directional RNNs we set $d_{\text{feat}} = h$ (hidden size), whereas for the bidirectional GRU we use $d_{\text{feat}} = 2h$. In every model we apply weight decay of 10^{-4} and Adam optimizer, learning rate 10^{-3}, batch size 128. The hyper-parameters used for each one were derived automatically.

- **GRU** (1-direction) - 0.29 M params. Two-layer GRU with hidden size 64 and inter-layer dropout 0.2. Only the final hidden state is forwarded to the regression head.
- **Bi-GRU** - 0.58 M params. Bidirectional architecture; the last forward and backward states are concatenated, doubling the feature dimension and giving the best empirical performance. As the best resulting approach, a full depiction of its hyper-parameter value selection

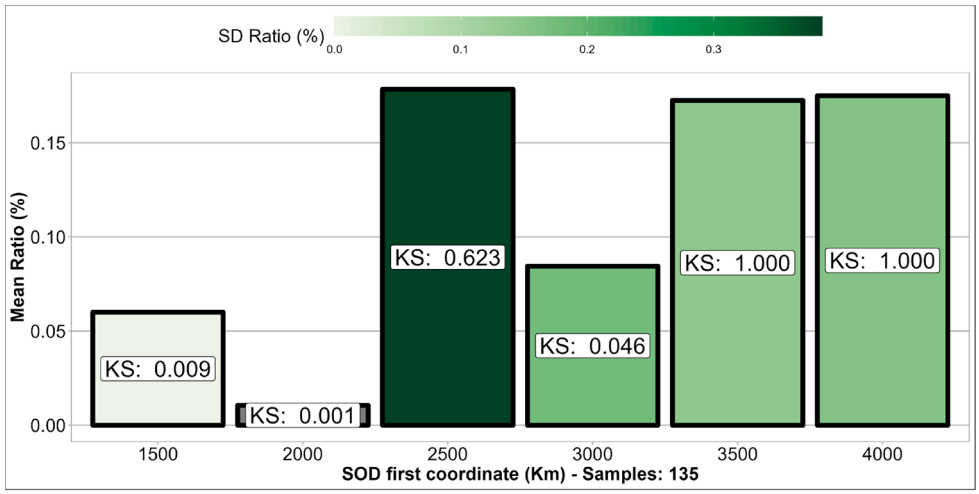

(a)

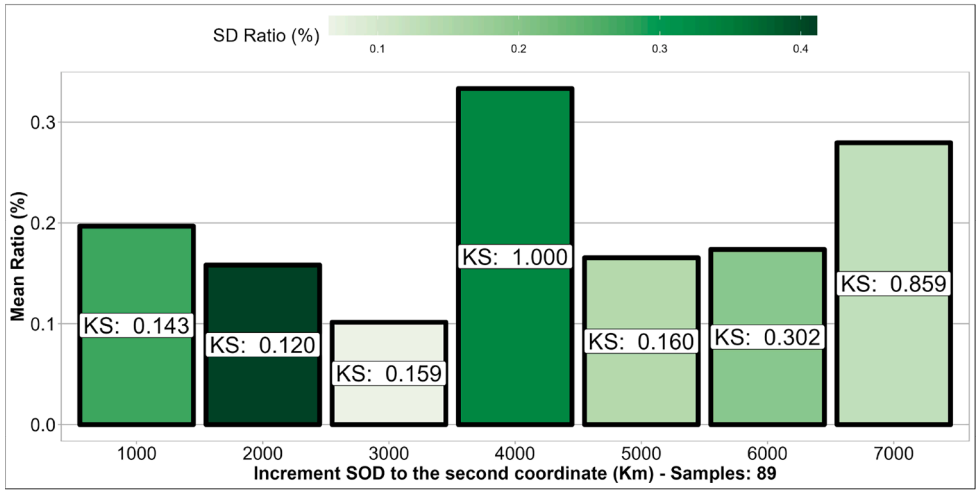

(b)

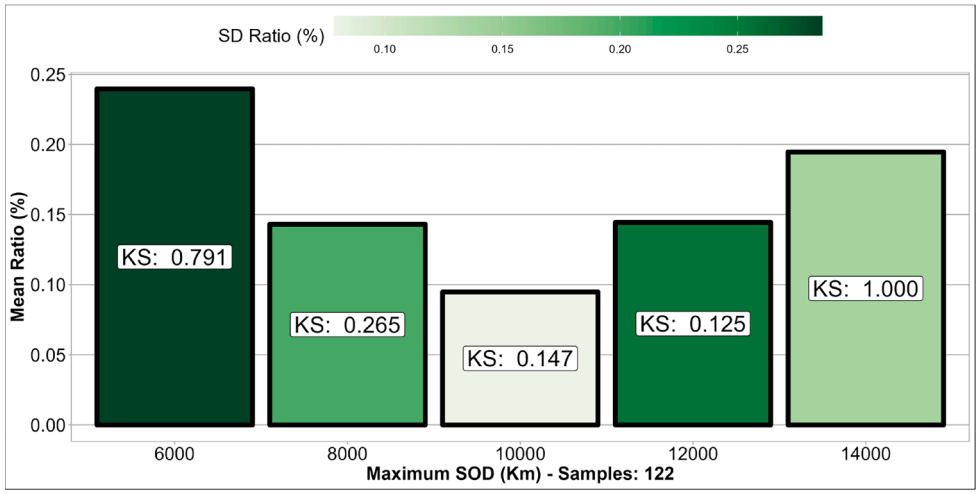

(c)

Fig. 9. Mean ratio obtained for each group. KS is the p-value of the KS test between selected group and the others. Color intensity represents the SD ratio. (a): Group based: Distance Start, reference KS: Distance Start = 4000. (b): Group based: EQ windows, reference KS: 24, filter to sequence length = 1200. (c): Group based: EQ windows, reference KS: 24, filter to sequence length = 1200.

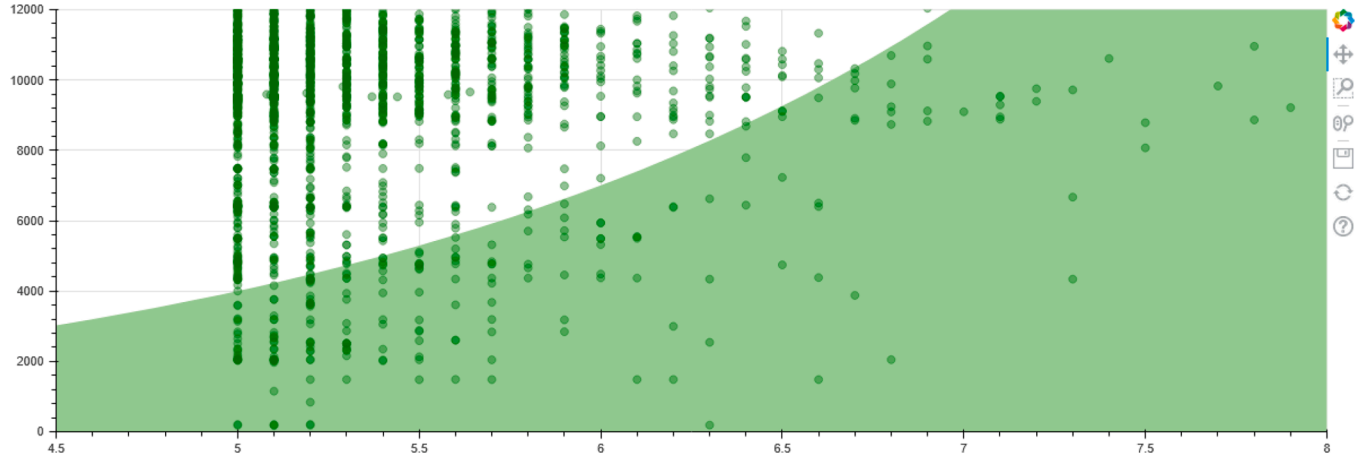

Fig. 10. SOD Magnitude coordinate space, Green points for EQ and green area for the selected EQs. x-axis: Magnitude, y-axis: SOD.

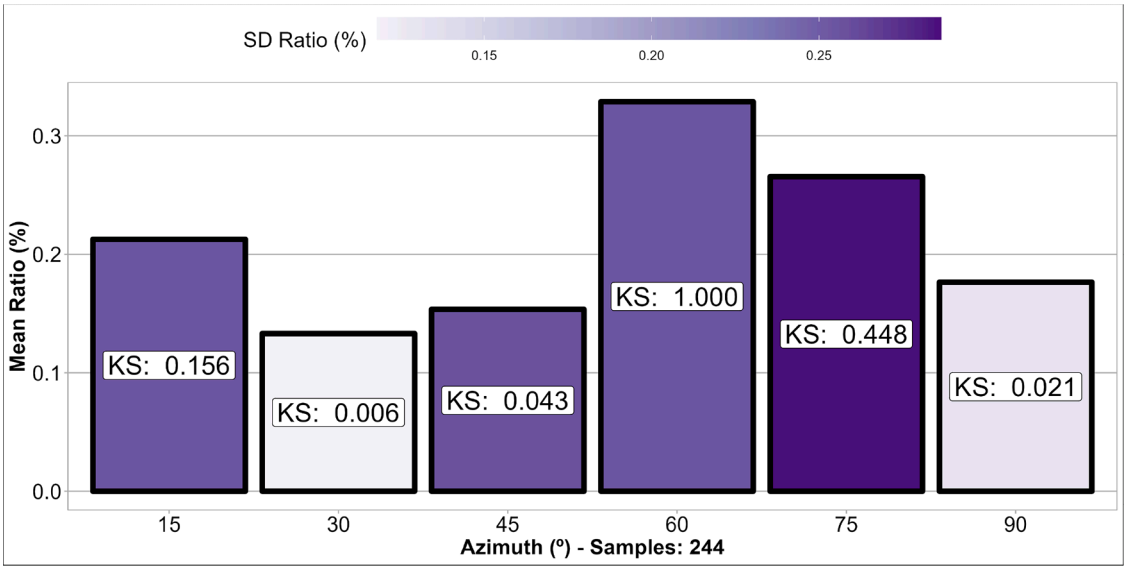

Fig. 11. Mean ratio obtained for each azimuth value from 15 to 90°. KS is the p-value of the KS test between an offset equal to 60 and the others. Color intensity represents the SD ratio.

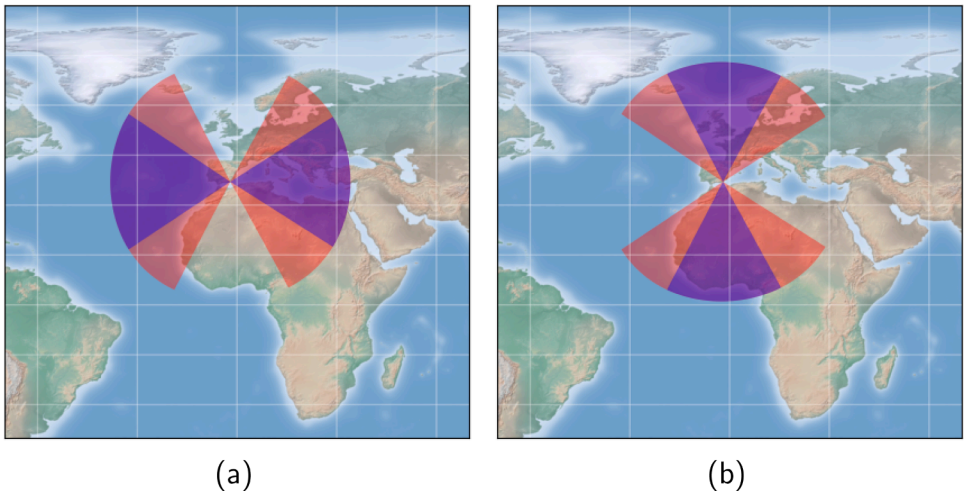

Fig. 12. EQ selection based on the azimuth maximum difference between the location of the observatory and the epicenter. Blue area: 30° maximum azimuth deviation, red area: 60° maximum azimuth deviation. (a) Aligned with the NS sensor, (b) perpendicular to the NS sensor.

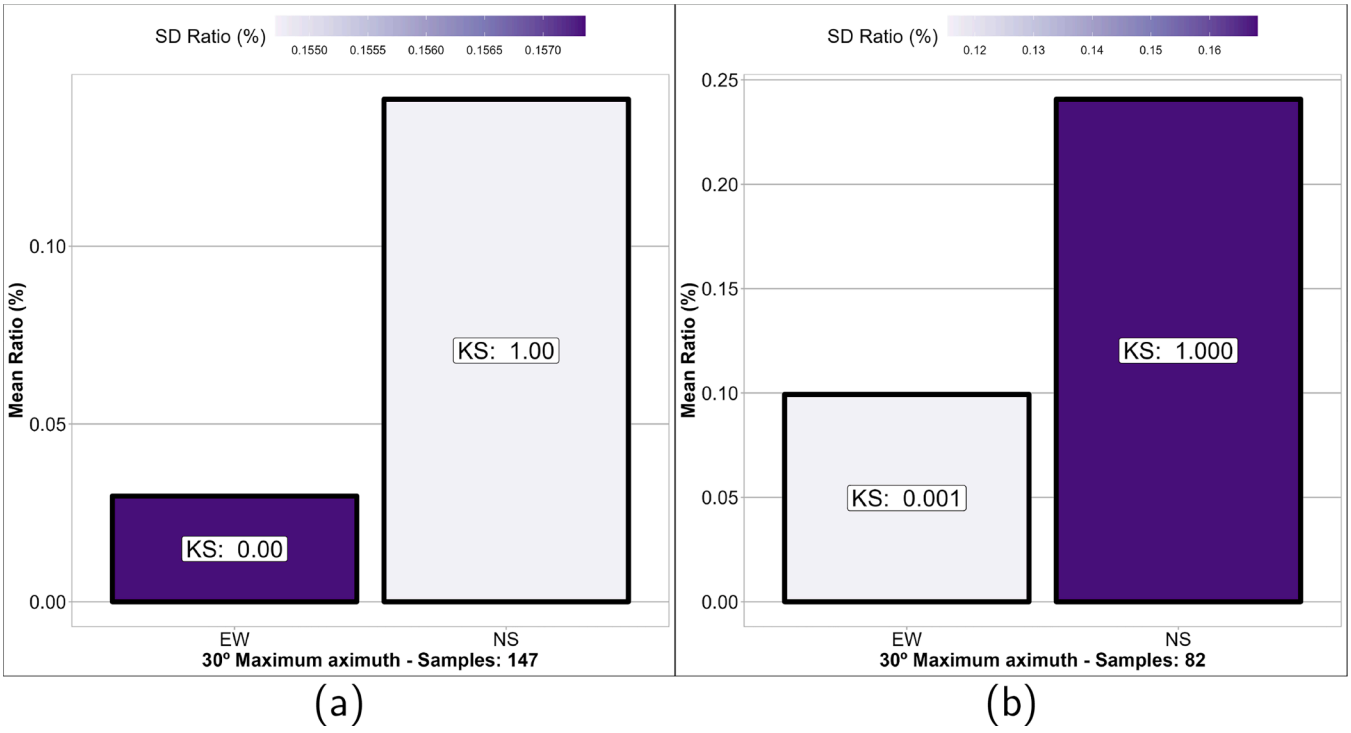

Fig. 13. Mean ratio obtained for each selection orientation EW and NS for two maximum values of azimuth (a) 30°, (b) 60°. KS is the p-value of the KS test between selected group and the others. Color intensity is the SD ratio.

with respect to the problem considered is given separately in subsection 5.4.2.

- **LSTM** - 0.31 M params. Two-layer LSTM (again $h=64$, dropout 0.2). We keep only the top-layer hidden state $\mathbf{h}_T$.
- **CNN-1D** - 44 k params. Three-layer CNN (kernel depth 16, 32, 64, size 10) and 2 fully-connected layers. Captures short-/mid-range patterns but struggles with long-term dependencies.
- **CNN-2D** - 46 k params. Identical layout in 2-D (kernel (10×1), stride (2×1)) applied on spectrogram-like inputs; otherwise mirrors the 1-D CNN. Performs poorly on very long sequences owing to limited receptive field.

The results can be seen in Fig. 14. The highest ratio value is obtained by the Bi-GRU architecture, although the GRU architecture also achieved satisfactory results. On the other hand, the CNN 1D and LSTM models performed considerably worse than the first two, with a higher value of SD. Surprisingly, the CNN 2D is not able to converge in any of the simulations.

The detection of EQ through SR signals is a complex task that can be assisted by the use of a specialized DL network, as it has been demonstrated in this paper. Despite the lack of systematic evidence of an effect on seismic signals, an appropriate DL network is capable of detecting some EQs in a long-term series. This is because RNN have the ability to analyze and learn from the time patterns in seismic signals, allowing them to detect events that manual inspection may miss. The ability of the network to both remember changes related to the event and forget the rest allows it to achieve EQ detection over time.

5.4.2. Hyper-parameter search and sensitivity analysis

To justify the choice of Bi-GRU settings (number of hidden units h, number of stacked layers L, and dropout probability p), we carried out an exhaustive grid search, followed by 10 independent re-runs of the best configuration. The search space comprised $h \in \{20, 50, 100, 150, 200\}$, $L \in \{1, 2, 3\}$ and $p \in \{0.0, 0.2, 0.5, 0.8\}$, yielding $5 \times 3 \times 4 = 60$ combinations. Each candidate was trained with five-fold cross-validation on the *train* + *val* split and ranked by the mean recognition ratio.

Fig. 15 (left) shows that $h = 150$ consistently attains the highest recognition ratio while also preserving a high test accuracy. Overall accuracy compares the predicted vector of the network with the ground truth output. Increasing h beyond 150 yields diminishing returns and, for $h = 200$, even a slight performance drop–suggesting overparameterization.

In the middle panel we observe a clear preference for a *single* Bi-GRU layer ($L = 1$), whereas deeper stacks ($L \geq 2$) systematically degrade both accuracy and recognition ratio. This indicates that a shallow recurrent backbone is sufficient, once bidirectional context is available.

Finally, the right-hand panel highlights a sweet spot at $p = .5$. Lower dropout (0.0 – 0.2) leads to mild overfitting, whereas aggressive regularisation ($p = .8$) impairs convergence.

The optimal triple $(h, L, p) = (150, 1, 0.5)$ was therefore selected for the final model. To verify robustness we re-trained this configuration ten times with different random seeds; the mean recognition ratio remained around **70 %**.

5.4.3. Comparison with a classical random forest baseline

To probe whether a carefully-tuned classical model could rival the sequence-aware Bi-GRU, we executed a 50-trial search that combines PCA for dimensionality reduction and a RF classifier. Each trial altered seven knobs:

1. **PCA components** $k \in [50, 300]$ – spectral sub-space fed to the forest,
2. **Number of trees** $n_{\text{est}} \in [200, 1200]$ – ensemble size,
3. **Maximum depth** $d_{\max} \in \{4, \ldots, 30, \text{None}\}$ – tree complexity,
4. **Min. samples split** $m_{\text{split}} \in [2, 10]$,
5. **Min. samples leaf** $m_{\text{leaf}} \in [1, 5]$ – both acting as regularisers,
6. **Feature subset** for node splits (*sqrt*, *log2*, or *all*), and
7. **Bootstrap** sampling (*on*/*off*).

Every candidate was scored with the recognition ratio on the same held-out validation windows used for the Bi-GRU evaluation.

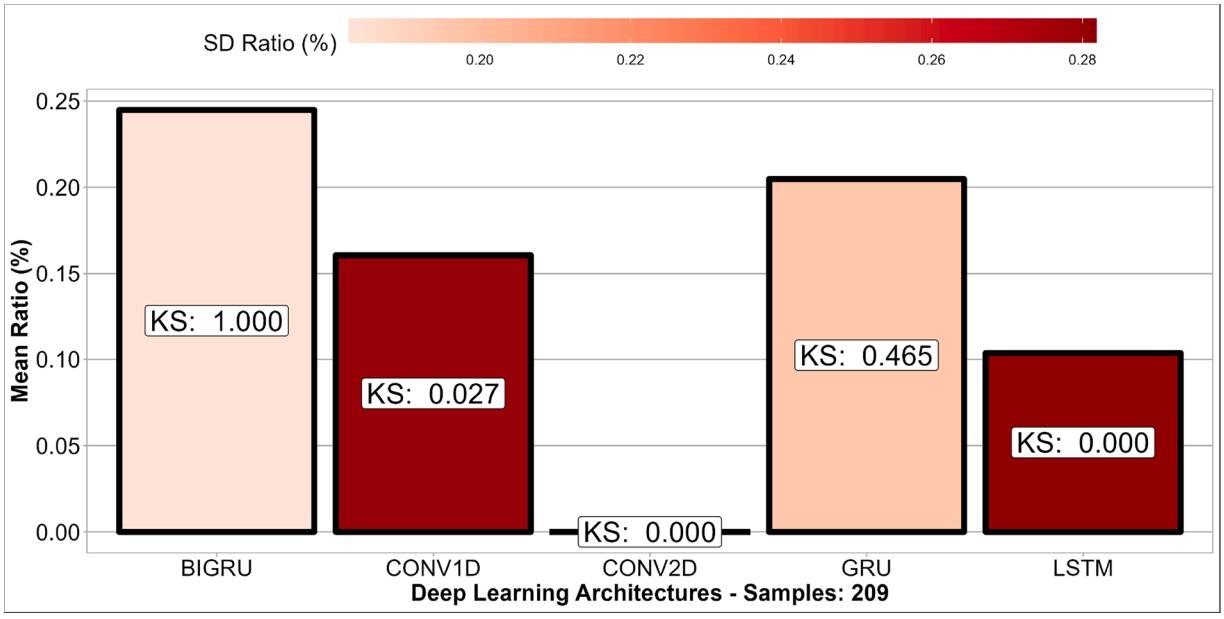

Fig. 14. Mean ratio obtained for the DL architecture proposed in this research. KS is the p-value of the KS test between the Bi-GRU group and the others. Color intensity represents the SD ratio.

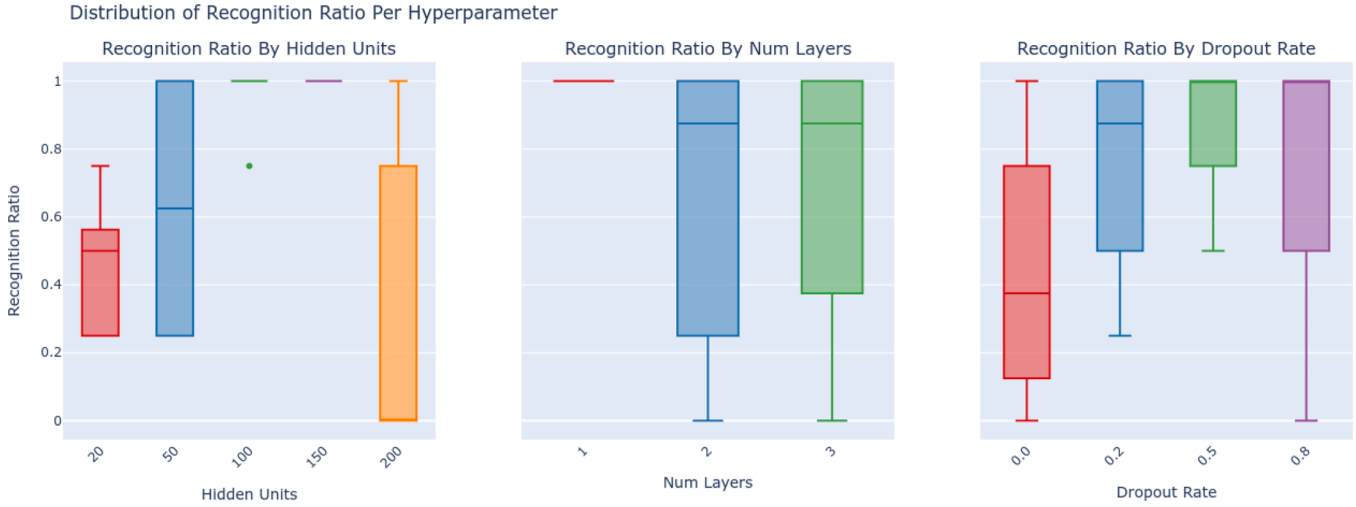

Fig. 15. Hyper-parameter impact on performance. **Left**: hidden units vs. recognition ratio; **Center**: number of GRU layers; **Right**: dropout rate. Boxes show inter-quartile range; black horizontal bars denote the mean.

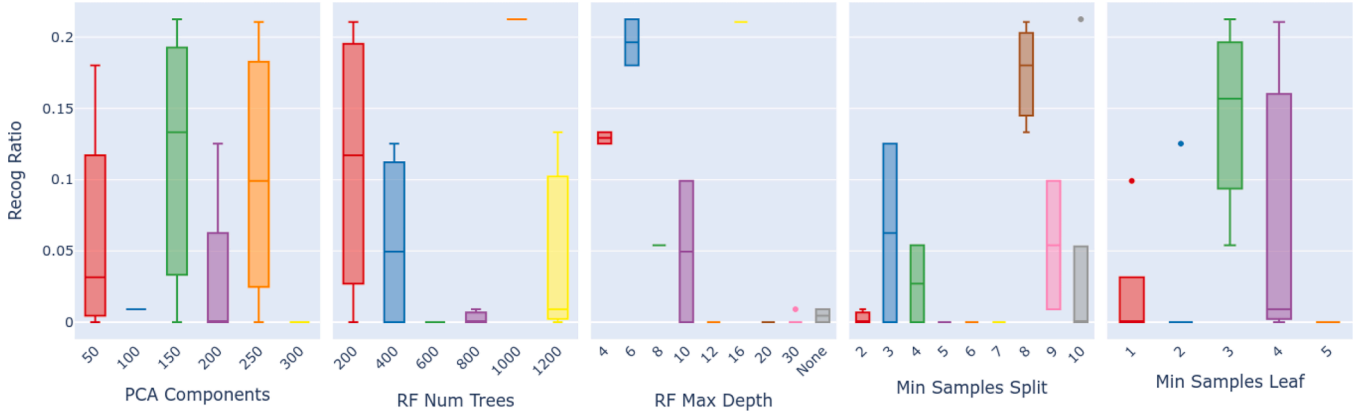

Fig. 16. Recognition-ratio obtained by each of the 20 tuned RF trials. Boxes show median and inter-quartile range for every tested value; whiskers span 1.5 IQR. Only one configuration exceeds 0.20.

Table 3
Held-out validation performance after RF hyper-parameter tuning versus the optimised Bi-GRU.

	RF (tuned)	Bi-GRU (best)
Input representation	960×10 *flatten*	960×10 sequence
PCA dimension k	150	–
Forest size / hidden units	1000 trees	–
Overall Accuracy	0.6 ± 0.02	0.72 ± 0.045
Recognition ratio	0.213 *(best)*	
	0.052 ± 0.078 *(mean)*	0.785 ± 0.015

Fig. 16 visualises the distribution of recognition ratios per hyper-parameter value. Results remain comparatively low for most settings: half of the trials yield virtually no recognised earthquakes. The single outlier ($k = 150$, $n_{\text{est}} = 1000$, $d_{\max} = 6$, $m_{\text{split}} = 10$, $m_{\text{leaf}} = 3$, no feature subsampling, no bootstrap) peaks at 0.213, yet raising tree count or depth beyond this point, or compressing further to $k = 50$, offering no benefit. The flat response confirms that model capacity is not the bottleneck; once the 9 600-D window is flattened, the temporal cues sought by the Bi-GRU are irretrievably lost.

Flattening each 20-minute Schumann-resonance window into a static vector strips away phase and lag relationships that manifest only across time steps. Consequently, even 1000 deep trees cannot discriminate the subtle pre-seismic signatures that a recurrent model captures through gated temporal dynamics. Although classical tuning improves RF results from 0.000 to 0.213, the gap to the Bi-GRU's 0.785 remains substantial, underscoring the need for explicitly temporal architectures in SR-based earthquake detection (Table 3).

6. Discussion

The model used in this research takes advantage of the recent developments on DL to expose several interesting effects related to the relationship between SR and EQ detection. Although a growing interest in this connection has been reached in recent years, the development of a DL detection model has not been proposed before.

6.1. Parameter selection

Different configurations of the several parameters contained in the model were explored. These configurations were tested looking mainly for two outcomes: to improve the performance of the model and to enhance the similarity between the EQ detector and their physical nature. The former is only interesting for this particular model. However, the latter can provide invaluable information to established evidence about the physical relationship between EQ and SR. In this discussion, these two aspects will be compared against each other. Explanatory models have been demonstrated as an effective method to understand the complex relationship inherent to intricate DL models. Using these techniques, it is possible to discern the most relevant parameters for the proposed model.

It has been stated that one observatory is not enough to detect all EQs, since the chance to detect their impact on the ionosphere depends on the proximity of the electromagnetic sensors to the epicenter. This implies that it is not possible to detect far away seismic movement with one station. However, this leads to the hypothesis that by aggregating several observatories it would be possible to geolocate the EQ epicenter based on SR measurements. This makes distance in which it is possible to detect EQ the most important variable in this model.

The length of the EQ windows, the maximum azimuth allowed, and the delta distance have obtained a very similar value of importance, which means that these variables contribute substantially. Contrary to the expectation, the sequence length does not reach a high value of importance; this can be explained by the fact that the other variables are determined to effectively detect the EQ, while the sequence length only improved the detection. These results are in line with the theoretical literature which relates the local state of the ionosphere with the frequency and Q-factor value of SR, both of them codified in the model input. On the other hand, the sequence length and EQ windows comparison offer an interesting evidence of the long-time dependency of the SR and EQ. However, these results are not completely conclusive, since the range of the different parameters makes it difficult to establish a unique criterion.

The parameter called offset, which is related to the position of the EQ occurrence in the segment, shows the best performance in the extreme values, and this can be explained by the bidirectional approach of the Bi-GRU model. The system is able to detect better when the EQ has been produced close to the end or the beginning of the sequence. The criteria used to establish which EQ can be perceived by an ELF observatory is under study, as it was explained in the introduction. In this respect, different strategies for selecting EQ have been followed, based on parameters using the perceptibility radius. The best outcomes, considering either mean value and SD, were presented in Fig. 10. The first conclusion to be drawn from these results is that the system can learn better when further away EQs are taken into account, as long as these EQs are particularly intense. The second conclusion is that considering just the nearest is not enough for the model to learn the EQ pattern. This fact can be explained because there are few EQs near the ELF observatory.

In our study, we empirically tested various distance thresholds to determine the optimal range for EQ detection using SR data. We found that a threshold of 14 000 km yielded the best model performance. This result is physically plausible: the Earth-ionosphere cavity supports global electromagnetic resonances with fundamental wavelengths of approximately 40 000 km, so an 14 000 km cap corresponds to just 0.2 λ and lies well within the first-order SR propagation regime.

Independent SR polarization studies report path-lengths of 10 500 km for individual ELF transients [63], while clear mode shifts up to ~3 000 km for moment magnitude [26]. Nonetheless, further external validation is warranted, and future work will investigate this threshold with additional multi-station data.

The azimuth selection provides precious information about the sensitivity of our sensors. Also, it supports the validity of the model, contrasting its performance when the same criteria for selecting the EQs related to the maximum azimuth are followed, but with two different approaches: one aligned with the maximum radiation pattern of the SR sensor and the other in the opposite alienation. Results show that performance deeply deteriorates when the selected EQs are not in line with the sensor sensitivity, reducing the success ratio by 3.

Although different DL models have been studied in a preliminary version of this research, five have been chosen to be compared in this paper. The GRU model has demonstrated to detect the EQ occurrence with the highest success ratio. In contrast, CNN 1D has detection capabilities in some cases, while the CNN 2D, which is similar to a codified spectrum, cannot detect under any circumstances the EQ occurrence. The criteria for the successful detection of some EQs by the network and its failure to detect others is beyond the scope of this article. However, a comprehensive analysis of each EQ will be thoroughly studied in future works.

This study deliberately focuses on the largest and closest EQs available to our station. They were chosen according to two deterministic criteria. The first is highest local impact: we ranked all events recorded during the study period by M_w and kept only those in the upper tail of the distribution. The second is station proximity: we retained only events whose epicenters fell inside the radius in which our single-station array maintains a favorable signal-to-noise ratio.

While this yields a small validation set, it maximizes waveform quality and offers a stringent proof-of-concept test for the proposed human-response sensing paradigm. The encouraging results must nevertheless be interpreted with caution: the model generalization to

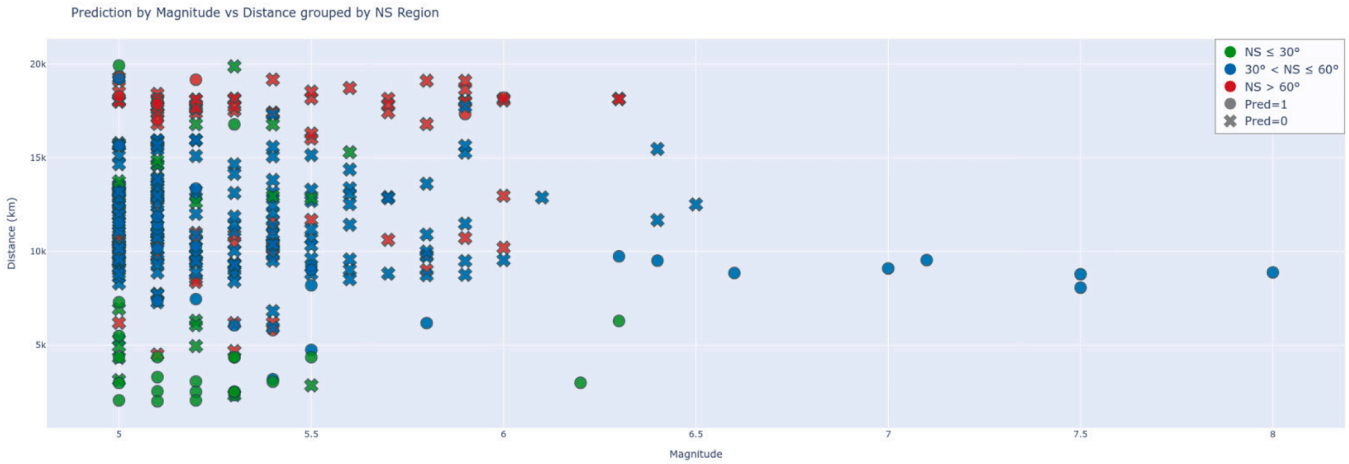

Fig. 17. Model predictions (filled circles: predicted = 1; crosses: predicted = 0) in the *training* set visualised in the magnitude-distance plane and colored by North-South (NS) region. Correct detections cluster at short epicentral distances (< 10 000 km) and/or higher magnitudes, indicating that the network has learned a physically plausible decision boundary.

weaker or more distant events remains unverified. Ongoing deployments at additional sites and an expanded catalogue will allow standard cross-validation and a thorough assessment of stability in future work.

6.2. Architecture rationale

The architectural choices for the two DL blocks are next summarized.

Spectral encoder. The three convolutional layers of the encoder employ a kernel size of 3 and stride 1 along the spectral axis, mirroring the ≈2 Hz spacing between adjacent Schumann-resonance modes within the 0–30 Hz band. Small kernels allow each filter to learn a *localised* resonance peak, while unit stride preserves the full spectral resolution (256 bins) required to track subtle frequency shifts. The feature map depths were established in our previous work as the best compromise between reconstruction fidelity and model size, and are retained here for consistency.

Temporal encoder. A systematic grid search[1] selected a *single-layer* BiGRU with 150 hidden units per direction and dropout $p = .5$. Hidden size 150 provides enough capacity to model the long-range evolution of SR codes, yet remains below the over-parameterization threshold observed for $h > 150$. Bidirectionality is crucial because the EQ offset within the 20s window is unknown; processing the sequence both forward and backward enables the network to detect perturbations that may appear near either edge. Ten independent re-runs of this configuration yield a mean recognition ratio of $\mathbf{78.5}\,\% \pm \mathbf{1.56}$, confirming its robustness.

6.3. Explainability analysis (XAI)

To dispel the "black-box" concern and to understand what the Bi-GRU actually learns, we applied SHapley Additive exPlanations (SHAP) to the full training set, where a sufficiently large number of EQ windows is available. Three complementary views are provided below.

Fig. 17 shows that true positives concentrate at distances below ∼10 000 km and, for larger distances, at magnitudes $M_w \gtrsim 6$. This pattern mirrors the empirical detectability surface discussed in Section 5 and confirms that the model is not over-fitting random noise.

The SHAP heat-map in Fig. 18 reveals strong, structured contributions from eight of the ten latent codes, while NS[0] and NS[7] remain near-neutral. Because each code captures a distinct spectral variation, the plot suggests that the detector relies on physically meaningful features rather than artefacts of the encoding.

Aggregating absolute SHAP values over the ten codes (Fig. 19) shows that the model pays most attention to the *beginning* and *end* of each 30-min segment, while the middle part is largely ignored. This behaviour is expected: SR perturbations caused by an EQ tend to be short-lived and therefore fall near the window edges after random offsetting (Section 3). The plot corroborates the physical interpretation that the detector is reacting to genuine transient signatures.

Taken together, these visualizations demonstrate that the DL model is not a pure black box: it learns a distance-magnitude relationship consistent with geophysical constraints, focuses on eight informative latent features, and localises its attention to plausible time spans within each register.

6.4. Comparison with traditional methods

Traditional EQ detection methods generally fall into seismic-based triggers, ionospheric precursors, and geochemical anomalies. Short-term seismic triggers, such as STA/LTA algorithms or network-based early-warning systems (e.g., ShakeAlert), achieve high detection probabilities (90–95 % for magnitudes $M \geq 4.5$) but provide little advance warning, detecting EQs within seconds after rupture onset. Regional methods utilizing ionospheric Total Electron Content (TEC) anomalies can offer hours to days of lead-time for large EQs ($M \geq 6$), but with moderate detection probabilities around 60–80 % and notable false positives related to geomagnetic activity. Geochemical indicators, particularly radon gas emissions, yield days-to-months lead-time but typically have lower detection probability (30–50 %) and sparse monitoring coverage.

In order to attain a quantitative comparison with traditional modalities, Table 4 collates representative values reported in the literature for three well-studied precursor channels: short-term seismic triggers (STA/LTA), ionospheric total-electron-content (TEC) anomalies, and geochemical radon emissions. Each modality trades detection probability against lead-time: STA/LTA achieves ≳90 % detection within seconds of rupture; TEC disturbances reach ∼hour-to-day horizons with magnitude-dependent hit rates ranging from 46 % ($M < 5$) to 100 % ($M > 6$); radon studies seldom exceed 70 % and suffer from sparse spatial coverage. Against this backdrop, our Schumann-resonance Bi-GRU delivers a preliminary recognition ratio of 78.5 % inside a ±12 h window, suggesting that SR-based monitoring could complement existing approaches in the moderate lead-time niche.

Compared to these classical approaches, our SR-based DL model targets a unique segment, providing moderate spatial coverage with po-

[1] 60 configurations, 5-fold cross-validation; details in Section 5.4.2.

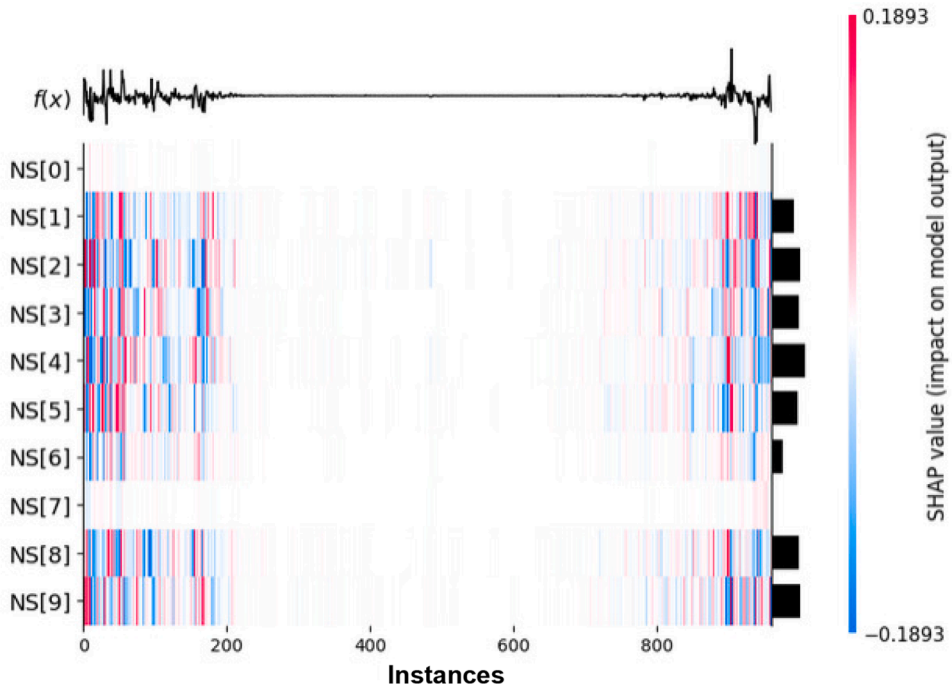

Fig. 18. Per-instance SHAP values for each latent code NS[0 – 9]. Red (blue) bars increase (decrease) the log-odds of an EQ window. The stacked histogram on the right-hand side emphasises that codes NS[1 – 6], NS[8] and NS[9] dominate the decision, whereas NS[0] and NS[7] contribute little.

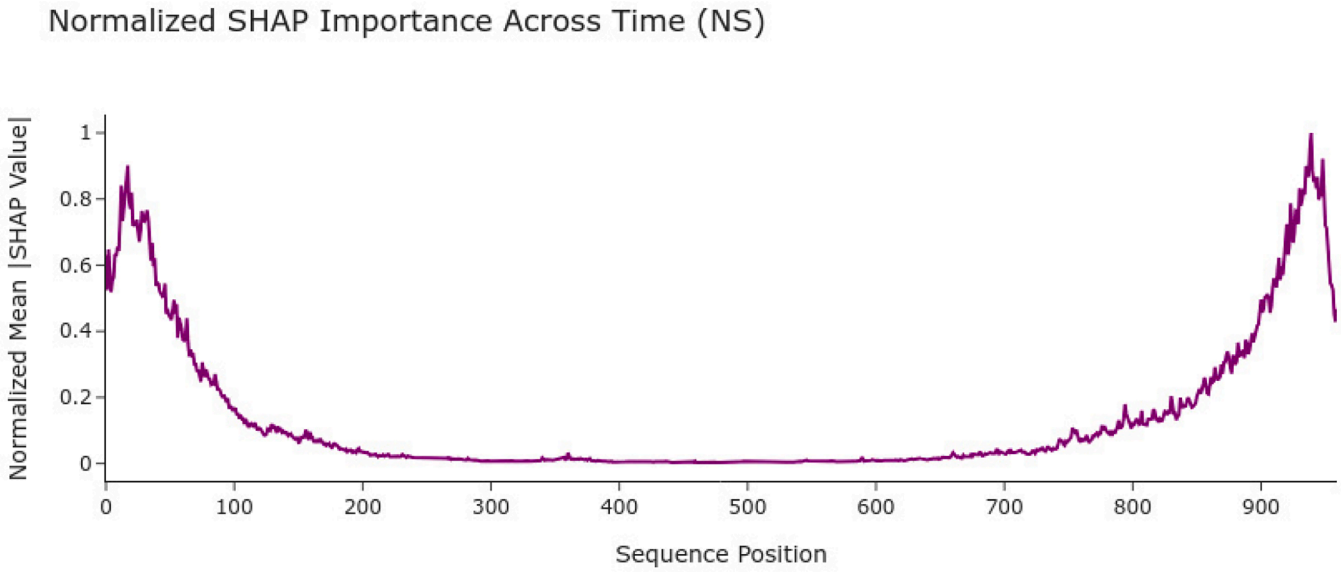

Fig. 19. Normalised mean |SHAP| across the 960-sample input sequence (0.5 h). The first and last ∼80 samples carry the highest importance, consistent with the bidirectional GRU focusing on the sequence edges where abrupt SR changes often occur.

Table 4
Illustrative detection performance reported for different precursor families. Values are taken from the cited studies and are *not* directly comparable across rows.

Modality	lead–time	detection prob.	Reference
Seismic STA/LTA trigger	1–10 s	90 %	[64]
Ionospheric TEC anomaly	30 min	46–100 %[a]	[65]
Radon emission anomaly	days	≤22 %	[66]
SR Bi-GRU (this work)	up to 24 h[b]	78.5 %	—

[a] Magnitude-dependent: 46.5 % for $M < 5$, 81.5 % for $5 \leq M < 6$, and 100 % for $M \geq 6$.

[b] Validation window spans ±12 h around each event.

tential early detection capabilities. Future comparative studies should evaluate precision and recall metrics within identical validation settings, determining optimal conditions under which SR-based methods outperform or complement traditional detection techniques.

We also added a RF baseline as a representative classical machine-learning technique. Despite a hyper-parameter procedure independent trainings, its mean recognition ratio was 0.213, sharply contrasting with the 0.785 achieved by our best Bi-GRU. The RF failure underscores the importance of models that explicitly exploit temporal dynamics; simple vectorization discards phase relationships indispensable for discriminating subtle Schumann-Resonance precursors.

7. Conclusions

To sum up, this work explores a potential solution for early warning of *Earthquake* (EQ) activity by analyzing the variations of the *Schumann Resonance* (SR) signal over a long period, taking advantage of the recent advances and power of *Deep Learning* (DL) models to reveal complicated patterns in physical phenomena. A deep *Artificial Intelligence* (AI) approach is proposed to detect perturbations of the steady patterns in intense lightning discharges associated with seismic activity.

Importantly, while the deep learning models employed here can act as black boxes, our sequential analysis of model architectures and parameters allows us to extract meaningful insights about the factors most relevant to EQ detection. We emphasize that enhancing model interpretability with dedicated explainable AI techniques–such as SHAP or Grad-CAM–is a promising avenue for future work, and we intend to pursue this in subsequent studies to further substantiate the physical relevance of the patterns learned by the DL models.

More than 20 Bi-GRU configurations were trained, logged, and statistically compared. The systematic grid search not only produced the best model (72 % overall accuracy, 78.5 % recognition ratio) but also reduced the risk of reporting a lucky hyper-parameter choice.

A classical *Random Forest* (RF) baseline was enhanced with a 50-trial Optuna hyper-parameter search combining PCA (50–300 components) and core forest parameters (200–1200 trees, depth 4–30, split rules, feature sampling, and bootstrap). Each SR window (960 × 10 samples) was flattened into a 9600-dimensional vector. The best RF configuration (150 PCA components, 1000 trees, depth 6, split 10, leaf 3, no feature sub-sampling, no bootstrap) reached a recognition ratio of **0.213**, with a mean of $\mathbf{0.05 \pm 0.078}$ across all trials. Despite this tuning gain, the RF remains well below the Bi-GRU's recognition ratio of **0.785**, underscoring the need for models that explicitly capture temporal dynamics.

This stark contrast confirms that (i) sequential context is crucial for capturing SR precursory signatures and (ii) naïve vectorisation of the signal is unable to exploit those dynamics.

The literature context lacking the generalization on the physical SR - EQ relationship gave way to examine several configurations of the parameters involved in the model and the criteria used to select EQs. The results of the different configurations of the model have been examined for similarity using the *Kolmogorov-Smirnov* (KS) test, to provide a quantitative index of each parameter performance.

From evaluating the significance of the different variables involved, the critical one is the maximum distance at which the model will consider EQs with a magnitude over five. The window size for EQ detection and the azimuth maximum difference are considered of moderate importance, along with the distance increments for an EQ of higher magnitude.

The successful application of a perceptibility radius to select the EQs from the magnitude-*Source-Observer Distance* (SOD) space also reflects the importance of these two variables, present in the analytical solutions used for the seismic wave, but adapted to the *Extremely Low Frequency* (ELF) signal analyzed by DL methods.

The azimuth maximum difference tests reveal the sensibility of the sensor to detect EQs in the area of the antenna's angular pattern. Verifying that perturbations introduced by EQs behave as the rest of the sources validates this detection methodology by distinctly recognizing the constraints of the physical relationship.

The results of this study provide empirical evidence about the validity of the proposed DL architecture. This approach joins the theoretical SR knowledge and the DL methods to explore the complex relationship between SR and EQ. This work may prove to be a stepping stone for further research with the aim to generalize the connection between seismic activity and SR records, while confirming the suitability of DL to solve intricate physical problems of signal processing.

The next step in the confirmation is our proof of concept is to test its generalization ability and statistical validity across several regions and sensor setups. In this respect, several future endeavors are targeted: (i) deploy identical sensors at two neighboring sites, (ii) expand the catalogue through data sharing with national agencies, and (iii) repeat the analysis with standard k-fold cross-validation once the enlarged data set becomes available.

CRediT authorship contribution statement

Carlos Cano-Domingo: Writing – review & editing, Writing – original draft, Visualization, Validation, Methodology, Investigation, Formal analysis, Conceptualization; **Ruxandra Stoean:** Writing – review & editing, Writing – original draft, Methodology, Investigation, Conceptualization; **Manuel Soler-Ortiz:** Validation, Investigation, Data curation; **Nuria Novas:** Validation, Resources, Data curation; **Manuel Fernández-Ros:** Validation, Resources, Data curation; **Gonzalo Joya:** Writing – review & editing, Methodology, Formal analysis; **Jose A. Gázquez Parra:** Validation, Resources, Data curation.

Data availability

Data will be made available on request.

Declaration of competing interest

The authors declare the following financial interests/personal relationships which may be considered as potential competing interests: Ruxandra Stoean reports financial support was provided by Executive Unit for Financing Higher Education Research Development and Innovation. Carlos Cano Domingo reports financial support was provided by Executive Unit for Financing Higher Education Research Development and Innovation. Nuria Novas reports financial support was provided by Ministry of Economics and Competitiveness of Spain. Manuel Fernandez-Ros reports financial support was provided by Ministry of Economics and Competitiveness of Spain. Jose Gazquez Parra reports financial support was provided by Ministry of Economics and Competitiveness of Spain. If there are other authors, they declare that they have no known competing financial interests or personal relationships that could have appeared to influence the work reported in this paper.

Acknowledgment

R. Stoean was supported by a grant of the Romanian Ministry of Research and Innovation, CCCDI - UEFISCDI, project number 178PCE/2021, PN-III-P4-ID-PCE-2020-0788, within PNCDI III. C. Cano was partially supported by a stay at the Electronics Technology Department of the University of Málaga. This research was also funded by CETPartnership, the European Partnership under Joint Call 2022 for research proposals, co-funded by the European Commission (GA N°101069750) and with the funding organisations listed on the CETPartnership website, project number COFUND-CETP 40/2024, UEFISCDI PNCDI IV. We also thank the Andalusian Institute of Geophysics. The Ministry of Economics and Competitiveness of Spain financed this work, under Project TEC2014-60132-P, in part by Innovation, Science and Enterprise, Andalusian Regional Government through the Electronics, Communications, and Telemedicine TIC019 Research Group of the University of Almeria, Spain and in part by the European Union FEDER Program and CIAMBITAL Group by I+D+I Project UAL18-TIC-A025-A, the University of Almeria, and the European Regional Development Fund (FEDER).

References

[1] R.A. Becerra-García, R.V. García-Bermúdez, G. Joya-Caparrós, A. Fernández-Higuera, C. Velázquez-Rodríguez, M. Velázquez-Mariño, F.R. Cuevas-Beltrán, F. García-Lagos, R. Rodráguez-Labrada, Data mining process for identification of non-spontaneous saccadic movements in clinical electrooculography, Neurocomputing 250 (2017) 28–36. https://doi.org/10.1016/j.neucom.2016.10.077

[2] C. Stoean, R. Stoean, M. Atencia, M. Abdar, L. Velázquez-Pérez, A. Khosravi, S. Nahavandi, U.R. Acharya, G. Joya, Automated detection of presymptomatic conditions in spinocerebellar ataxia type 2 using Monte Carlo dropout and deep neural network techniques with electrooculogram signals, Sensors 20 (11) (2020). https://doi.org/10.3390/s20113032

[3] X. Wang, V. Liesaputra, Z. Liu, Y. Wang, Z. Huang, An in-depth survey on deep learning-based motor imagery electroencephalogram (EEG) classification, Artif. Intell. Med. 147 (2024) 102738. https://doi.org/10.1016/j.artmed.2023.102738

[4] N.N. Jose, G. Deipali, G. Vivekanandan, E. Nithya, V. Nallarasan, K. Krishnakumar, Efficient predefined time adaptive neural network for motor execution EEG signal classification based brain-computer interaction, Knowl. Based Syst. 303 (2024) 112270. https://doi.org/10.1016/j.knosys.2024.112270

[5] R. Natras, B. Soja, M. Schmidt, Machine learning ensemble approach for ionosphere and space weather forecasting with uncertainty quantification, 2022 3rd URSI Atlantic and Asia Pacific Radio Science Meeting (AT-AP-RASC) (2022) 1–4. https://doi.org/10.23919/AT-AP-RASC54737.2022.9814334

[6] K. Sivakrishna, D.V. Ratnam, G. Sivavaraprasad, A bidirectional deep-learning algorithm to forecast regional ionospheric TEC maps, IEEE J. Sel. Top. Appl. Earth Obs. Remote Sens. 15 (2022) 4531–4543. https://doi.org/10.1109/JSTARS.2022.3180940

[7] T. Fu, C. Wang, N. Cheng, Deep-learning-based joint optimization of renewable energy storage and routing in vehicular energy network, IEEE Internet Things J. 7 (2020) 6229–6241. https://doi.org/10.1109/JIOT.2020.2966660

[8] H. Wang, Z. Lei, X. Zhang, B. Zhou, J. Peng, A review of deep learning for renewable energy forecasting, Energy Convers. Manage. 198 (2019) 111799. https://doi.org/10.1016/j.enconman.2019.111799

[9] P.K. Shukla, K. Deepa, Deep learning techniques for transmission line fault classification - a comparative study, Ain Shams Eng. J. 15 (2) (2024) 102427. https://doi.org/10.1016/j.asej.2023.102427

[10] J.A. Gazquez, R.M. Garcia, N.N. Castellano, M. Fernandez-Ros, A.J. Perea-Moreno, F. Manzano-Agugliaro, Applied engineering using schumann resonance for earthquakes monitoring, Appl. Sci. 7 (11) (2017). https://doi.org/10.3390/app7111113

[11] C. Cano-Domingo, R. Stoean, G. Joya, N. Novas, M. Fernandez-Ros, J.A. Gazquez, A machine learning hourly analysis on the relation the ionosphere and schumann resonance frequency, Measurement 208 (2023) 112426. https://doi.org/10.1016/j.measurement.2022.112426

[12] A. Pizzuti, A. Bennett, M. Füllekrug, Long-term observations of schumann resonances at portishead (UK), Atmosphere 13 (2022). https://doi.org/10.3390/atmos13010038

[13] A.V. Koloskov, A.P. Nickolaenko, Y.M. Yampolsky, C. Hall, O.V. Budanov, Variations of global thunderstorm activity derived from the long-term schumann resonance monitoring in the antarctic and in the arctic, J. Atmos. Sol. Terr. Phys. 201 (February) (2020) 105231. https://doi.org/10.1016/j.jastp.2020.105231

[14] G. Tatsis, V. Christofilakis, S.K. Chronopoulos, G. Baldoumas, A. Sakkas, A.K. Paschalidou, P. Kassomenos, I. Petrou, P. Kostarakis, C. Repapis, V. Tritakis, Study of the variations in the schumann resonances parameters measured in a southern Mediterranean environment, Sci. Total Environ. 715 (2020). https://doi.org/10.1016/j.scitotenv.2020.136926

[15] M. Pazos, B. Mendoza, P. Sierra, E. Andrade, D. Rodríguez, V. Mendoza, R. Garduño, Analysis of the effects of geomagnetic storms in the schumann resonance station data in Mexico, J. Atmos. Sol. Terr. Phys. 193 (2019) 105091. https://doi.org/10.1016/j.jastp.2019.105091

[16] G. Sátori, E. Williams, C. Price, R. Boldi, A. Koloskov, Y. Yampolski, A. Guha, V. Barta, Effects of energetic solar emissions on the earth-ionosphere cavity of schumann resonances, Surv. Geophys. 37 (4) (2016) 757–789. https://doi.org/10.1007/s10712-016-9369-z

[17] T. Bozóki, E. Prácser, G. Sátori, G. Dálya, K. Kapás, J. Takátsy, et al., Modeling schumann resonances with schupy, J. Atmos. Sol. Terr. Phys. 196 (October) (2019). https://doi.org/10.1016/j.jastp.2019.105144

[18] I. Hetita, A.S. Zalhaf, D.-E.A. Mansour, Y. Han, P. Yang, C. Wang, Accurate modeling of photovoltaic systems for studying the transient effects of lightning strikes, Energy Rep. 8 (2022) 429–438. 2021 The 8th International Conference on Power and Energy Systems Engineering. https://doi.org/10.1016/j.egyr.2021.11.111

[19] O. Akdag, Strengthening distribution systems after earthquakes with a new analytical model, Electr. Power Syst. Res. 232 (2024) 110337. https://doi.org/10.1016/j.epsr.2024.110337

[20] T. Divett, M. Ingham, G. Richardson, M. Sigley, C. Rodger, Modeling pipe to soil potentials from geomagnetic storms in gas pipelines in New Zealand, Space Weather 21 (2023). https://doi.org/10.1029/2023SW003601

[21] W.-F. Chen, E.M. Lui, Earthquake Engineering for Structural Design, CRC Press, 2005.

[22] X. Jin, L. Zhang, J. Bu, G. Qiu, L. Ma, C. Liu, Y. Li, Discussion on anomaly of atmospheric electrostatic field in wenchuan ms8.0 earthquake, J. Electrostat. 104 (2020) 103423. https://doi.org/10.1016/j.elstat.2020.103423

[23] D. Recchiuti, G. D'Angelo, E. Papini, P. Diego, A. Cicone, A. Parmentier, P. Ubertini, R. Battiston, M. Piersanti, Detection of electromagnetic anomalies over seismic regions during two strong (MW > 5) earthquakes, Front. Earth Sci. 11 (2023). https://doi.org/10.3389/feart.2023.1152343

[24] W.O. Schumann, Über die strahlungslosen eigenschwingungen einer leitenden kugel, die von einer luftschicht und einer ionosphärenhülle umgeben ist, Zeitschrift fur Naturforschung - Sec. A J. Phys. Sci. 7 (2) (1952) 149–154. https://doi.org/10.1515/zna-1952-0202

[25] A. Nickolaenko, M. Hayakawa, Schumann Resonance for Tyros: Essentials of Global Electromagnetic Resonance in the Earth-Ionosphere Cavity, Springer, Tokyo, 2014. https://doi.org/10.1007/978-4-431-54358-9

[26] Y.P. Galuk, I.G. Kudintseva, A.P. Nickolaenko, M. Hayakawa, Modifications of schumann resonance spectra as an estimate of causative earthquake magnitude: the model treatment, J. Atmos. Sol. Terr. Phys. 209 (2020). https://doi.org/10.1016/j.jastp.2020.105392

[27] T. Ogawa, Y. Tanaka, Q factors of the schumann resonances and solar activity, Special Contrib. Geophys. Inst. Kyoto Univer. 10 (1970) 21–28.

[28] C. Cano-Domingo, R. Stoean, N. Novas-Castellano, M. Fernandez-Ros, G. Joya, J.A. Gazquez-Parra, On the prospective use of deep learning systems for earthquake forecasting over schumann resonances signals, in: Engineering Proceedings, MDPI AG, 2022, p. 15. https://doi.org/10.3390/engproc2022018015

[29] G. Cremen, C. Galasso, Earthquake early warning: recent advances and perspectives, Earth Sci. Rev. 205 (2020). https://doi.org/10.1016/j.earscirev.2020.103184

[30] J.B. Rundle, A. Donnellan, G. Fox, J.P. Crutchfield, Nowcasting earthquakes by visualizing the earthquake cycle with machine learning: a comparison of two methods, Surv. Geophys. 43 (2022) 483–501. https://doi.org/10.1007/s10712-021-09655-3

[31] Y. Xie, M.E. Sichani, J.E. Padgett, R. DesRoches, The promise of implementing machine learning in earthquake engineering: a state-of-the-art review, Earthquake Spectra 36 (2020) 1769–1801. https://doi.org/10.1177/8755293020919419

[32] F. Jing, R.P. Singh, X. Shen, Land-atmosphere-meteorological coupling associated with the 2015 Gorkha (m 7.8) and dolakha (m 7.3) Nepal earthquakes, Geomatics Natural Hazards Risk 10 (2019) 1267–1284. https://doi.org/10.1080/19475705.2019.1573629

[33] F. Jing, R.P. Singh, Response of surface and atmospheric parameters associated with the Iran m 7.3 earthquake, IEEE J. Sel. Top. Appl. Earth Obs. Remote Sens. 15 (2022) 5841–5852. https://doi.org/10.1109/JSTARS.2022.3188003

[34] X. Shen, X. Zhang, L. Wang, H. Chen, Y. Wu, S. Yuan, J. Shen, S. Zhao, J. Qian, J. Ding, The earthquake-related disturbances in ionosphere and project of the first China seismo-electromagnetic satellite, Earthquake Sci. 24 (2011) 639–650. https://doi.org/10.1007/s11589-011-0824-0

[35] V. Tritakis, J. Mlynarczyk, I. Contopoulos, J. Kubisz, V. Christofilakis, G. Tatsis, S.K. Chronopoulos, C. Repapis, Extremely low frequency (ELF) electromagnetic signals as a possible precursory warning of incoming seismic activity, Atmosphere 15 (4) (2024). https://doi.org/10.3390/atmos15040457

[36] S. Jin, G. Occhipinti, R. Jin, GNSS Ionospheric seismology: recent observation evidences and characteristics, Earth Sci. Rev. 147 (2015) 54–64. https://doi.org/10.1016/j.earscirev.2015.05.003

[37] J. Witt, Predicting earthquakes by monitoring the ionosphere, 2023, http://www.ll.mit.edu/news/predicting-earthquakes-monitoring-ionosphere. [Online; accessed 17-February-2025].

[38] X. Zhang, J. Liu, A. De Santis, L. Perrone, P. Xiong, X. Zhang, X. Du, Lithosphere-atmosphere-ionosphere coupling associated with four yutian earthquakes in China from GPS TEC and electromagnetic observations onboard satellites, J. Geodyn. 155 (2023) 101943. https://doi.org/10.1016/j.jog.2022.101943

[39] D. Marchetti, K. Zhu, A. Piscini, E. Ghamry, X. Shen, R. Yan, X. He, T. Wang, W. Chen, J. Wen, Y. Zhang, Y. Cheng, M. Fan, D. Zhang, H. Zhang, G. Ventura, Changes in the lithosphere, atmosphere, and ionosphere before and during the mw = 7.7 jamaica 2020 earthquake, Remote Sens Environ 307 (2024) 114146. https://doi.org/10.1016/j.rse.2024.114146

[40] L. Feng, W. Zhu, Y. Guan, W. Fan, Y. Ji, A new method for extracting geomagnetic perturbation anomalies preceding the M7.4 Maduo earthquake, Phys. Earth Planet. Inter. 359 (2025) 107305. https://doi.org/10.1016/j.pepi.2024.107305

[41] A. Hameed, M. Shah, B. Ghaffar, S. Riaz, P. Jamjareegulgarn, N.S. Alarifi, M.R. Abukhadra, Possible atmospheric-ionospheric precursors of the 2020 hotan China earthquake from various satellites, Adv. Space Res. 74 (7) (2024) 3326–3343. https://doi.org/10.1016/j.asr.2024.06.016

[42] P. Xiong, C. Long, H. Zhou, X. Zhang, X. Shen, GNSS TEC-based earthquake ionospheric perturbation detection using a novel deep learning framework, IEEE J. Sel. Top. Appl. Earth Obs. Remote Sens. 15 (2022) 4248–4263. https://doi.org/10.1109/JSTARS.2022.3175961

[43] A. Cofré, M. Marín, O.V. Pino, N. Galleguillos, S. Riquelme, S. Barrientos, N.B. Yoma, End-to-end LSTM-based earthquake magnitude estimation with a single station, IEEE Geosci. Remote Sens. Lett. 19 (2022) 1–5. https://doi.org/10.1109/LGRS.2022.3175108

[44] M.S. Abdalzaher, M.S. Soliman, S.M. El-Hady, A. Benslimane, M. Elwekeil, A deep learning model for earthquake parameters observation in IoT system-based earthquake early warning, IEEE Internet Things J. 9 (2022) 8412–8424. https://doi.org/10.1109/JIOT.2021.3114420

[45] O.M. Saad, A.G. Hafez, M.S. Soliman, Deep learning approach for earthquake parameters classification in earthquake early warning system, IEEE Geosci. Remote Sens. Lett. 18 (2021) 1293–1297. https://doi.org/10.1109/LGRS.2020.2998580

[46] O.M. Saad, Y. Chen, D. Siervo, F. Zhang, A. Savvaidis, G.-c.D. Huang, N. Igonin, S. Fomel, Y. Chen, EQCCT: A production-ready earthquake detection and phase-picking method using the compact convolutional transformer, IEEE Trans. Geosci. Remote Sens. 61 (2023) 1–15. https://doi.org/10.1109/TGRS.2023.3319440

[47] A. Licciardi, Q. Bletery, B. Rouet-Leduc, J.P. Ampuero, K. Juhel, Instantaneous tracking of earthquake growth with elastogravity signals, Nature 606 (2022) 1–6. https://doi.org/10.1038/s41586-022-04672-7

[48] M. Hayakawa, J. Izutsu, A.Y. Schekotov, A.P. Nickolaenko, Y.P. Galuk, I.G. Kudintseva, et al., Anomalies of schumann resonances as observed near nagoya associated with two huge (M7) tohoku offshore earthquakes in 2021, J. Atmos. Sol. Terr. Phys. 225 (2021). https://doi.org/10.1016/j.jastp.2021.105761

[49] P.S. Figueredo, B.M. Ortega, M. Pazos, D.R. Osorio, E.A. Mascote, V.M. Mendoza, R. Garduño, Schumann resonance anomalies possibly associated with large earthquakes in mexico, Indian J. Phys. 95 (2021) 1959–1966. https://doi.org/10.1007/s12648-020-01865-6

[50] V. Christofilakis, G. Tatsis, C. Votis, I. Contopoulos, C. Repapis, V. Tritakis, Significant ELF perturbations in the schumann resonance band before and during a shallow mid-magnitude seismic activity in the greek area (kalpaki), J. Atmos. Sol. Terr. Phys. 182 (2019) 138–146. https://doi.org/10.1016/j.jastp.2018.11.009
[51] V. Tritakis, I. Contopoulos, J. Mlynarczyk, V. Christofilakis, G. Tatsis, C. Repapis, How effective and prerequisite are electromagnetic extremely low frequency (ELF) recordings in the schumann resonances band to function as seismic activity precursors, Atmosphere 13 (2022). https://doi.org/10.3390/atmos13020185
[52] C. Cano Domingo, M. Fernandez Ros, N. Novas Castellano, J.A.G. Parra, Diurnal and seasonal results of the schumann resonance observatory in sierra de filabres, spain, IEEE Trans. Antennas Propag. 69 (10) (2021) 6680–6690. https://doi.org/10.1109/TAP.2021.3069537
[53] C. Cano-Domingo, R. Stoean, G. Joya, N. Novas, M. Fernandez-Ros, J.A. Gazquez Parra, A hybrid deep learning approach for enhancing the Lorentzian curve fit algorithm for Schumann resonance, Expert Syst. Appl. 293 (2025) 128681. https://doi.org/10.1016/j.eswa.2025.128681
[54] A. Shrestha, A. Mahmood, Review of deep learning algorithms and architectures, IEEE Access 7 (2019) 53040–53065. https://doi.org/10.1109/ACCESS.2019.2912200
[55] Z. Wang, X. Xu, W. Zhang, G. Trajcevski, T. Zhong, F. Zhou, Learning latent seasonal-trend representations for time series forecasting, in: S. Koyejo, S. Mohamed, A. Agarwal, D. Belgrave, K. Cho, A. Oh (Eds.), Advances in Neural Information Processing Systems, volume 35, Curran Associates, Inc., 2022, pp. 38775–38787.
[56] H. Dou, P. Shi, Y. Zhang, P. Chen, Z. Zheng, Deanomaly: anomaly detection for multivariate time series using robust decomposition and memory-augmented diffusion models, IEEE Trans. Instrum. Meas. 74 (2025) 1–14. https://doi.org/10.1109/TIM.2025.3570337
[57] Lists, maps, and statistics | u.s. geological survey, 2021. https://www.usgs.gov/programs/earthquake-hazards/lists-maps-and-statistics.
[58] F. Magrini, D. Jozinović, F. Cammarano, A. Michelini, L. Boschi, Local earthquakes detection: a benchmark dataset of 3-component seismograms built on a global scale, Artif. Intell. Geosci. 1 (2020) 1–10. https://doi.org/10.1016/j.aiig.2020.04.001
[59] V.W. Berger, Y. Zhou, Kolmogorov–Smirnov Test: Overview, Wiley statsref: Statistics reference online (2014).
[60] G. Ridgeway, Generalized boosted models: a guide to the gbm package, Update 1 (1) (2007) 2007.
[61] P. Biecek, Dalex: explainers for complex predictive models in r, J. Mach. Learn. Res. 19 (1) (2018) 3245–3249.
[62] K. Umeda, N. Watanabe, M. Hayakawa, ULF/ELF Emissions observed in Japan, possibly associated with the chi-Chi earthquake in Taiwan, Nat. Hazard. Earth Syst. Sci. 1 (2001). https://doi.org/10.5194/nhess-1-37-2001
[63] A. Tzanis, D. Beamish, Time domain polarization analysis of schumann resonance waveforms, J. Atmos. Terr. Phys. 49 (3) (1987) 217–229. https://doi.org/10.1016/0021-9169(87)90057-2
[64] A.I. Lux, D. Smith, M. Böse, J.J. McGuire, J.K. Saunders, M. Huynh, I. Stubailo, J. Andrews, G. Lotto, B. Crowell, S. Crane, R.M. Allen, D. Given, R. Hartog, T. Heaton, A. Husker, J. Marty, L. O'Driscoll, H. Tobin, S.K. McBride, D. Toomey, Status and performance of the shakealert earthquake early warning system: 2019–2023, Bull. Seismol. Soc. Am. 114 (6) (2024) 3041–3062. https://doi.org/10.1785/0120230259
[65] P. Picozza, L. Conti, A. Sotgiu, Looking for earthquake precursors from space: A critical review, 2021. https://doi.org/10.3389/feart.2021.676775
[66] H. Woith, Radon earthquake precursor: a short review, 2015. https://doi.org/10.1140/epjst/e2015-02395-9